

Water mass pathways to the North Atlantic

Oxygen Minimum Zone

Jesús Peña-Izquierdo, Institut de Ciències del Mar, ICM-CSIC, Passeig Marítim de la Barceloneta, 37-49, Barcelona, Spain. (Corresponding author: susope@icm.csic.es)

Erik van Sebille, Climate Change Research Centre and ARC Centre of Excellence for Climate System Science, UNSW, Sydney, Australia (now at Grantham Institute & Department of Physics, Imperial College, London, United Kingdom)

Josep L. Pelegrí, Institut de Ciències del Mar, ICM-CSIC, Passeig Marítim de la Barceloneta, 37-49, Barcelona, Spain.

Janet Sprintall, Scripps Institution of Oceanography, UCSD, 9500 Gilman Drive, La Jolla, CA 92093, USA.

Evan Mason, Instituto Mediterráneo de Estudios Avanzados, IMEDEA-CSIC, C/ Miquel Marqués, 21, 07190 Esporles, Spain.

Pedro J. Llanillo, Institut de Ciències del Mar, ICM-CSIC, Passeig Marítim de la Barceloneta, 37-49, Barcelona, Spain.

Francisco Machín, InvestigAdHoc S.A. , C/ Andalucía 2, 35210 Telde, Spain

29 **Abstract**

30

31 The water mass pathways to the North Atlantic Oxygen Minimum Zone (naOMZ) are
32 traditionally sketched within the cyclonic tropical circulation via the poleward
33 branching from the eastward flowing jets that lie south of 10°N. However, our water
34 mass analysis of historic hydrographic observations together with numerical Lagrangian
35 experiments consistently reveal that the potential density level of $\sigma_\theta = 26.8 \text{ kg m}^{-3}$
36 ($\sigma_{26.8}$, approximately 300 m depth) separates two distinct regimes of circulation within
37 the Central Water (CW) stratum of the naOMZ. In the upper CW (above $\sigma_{26.8}$), and in
38 agreement with previous studies, the supply of water mainly comes from the south with
39 a predominant contribution of South Atlantic CW. In the lower CW (below $\sigma_{26.8}$),
40 where minimal oxygen content is found, the tropical pathway is instead drastically
41 weakened in favour of a subtropical pathway. More than two thirds of the total water
42 supply to this lower layer takes place north of 10°N, mainly via an eastward flow at
43 14°N and northern recirculations from the northern subtropical gyre. The existence of
44 these northern jets explains the greater contribution of North Atlantic CW observed in
45 the lower CW, making up to 50% of the water mass at the naOMZ core. The
46 equatorward transfer of mass from the well-ventilated northern subtropical gyre
47 emerges as an essential part of the ventilation of the naOMZ.

48

49

50

51 **1. Introduction**

52
53 The classical theory on thermocline ventilation [*Luyten et al.*, 1983] postulates the
54 existence of regions at the eastern margin of the ocean isolated from the wind-driven
55 circulation. A sluggish circulation characterizes these so-called shadow zones that are
56 located between the well-ventilated subtropical gyres and the tropical system of zonal
57 jets. In addition to the weak ventilation, the microbial respiration of the organic matter
58 from the nearby highly productive coastal upwelling system leads to the development of
59 oxygen minimum zones (OMZs) between 100 and 900 m depths, thus within Central
60 Water (CW) and Intermediate Water (IW) strata [*Karstensen et al.*, 2008].

61
62 All OMZs present hypoxic conditions under which most marine species cannot survive
63 [*Vaquier-Sunyer and Duarte*, 2008]. Moreover, oxygen also plays an essential role in
64 biogeochemical processes, such as in the nitrogen and carbon cycles [*Bopp et al.*, 2002;
65 *Lam and Kuypers*, 2011; *Paulmier et al.*, 2011], with a direct impact on climate
66 dynamics. Several decades of observations have revealed that the world ocean OMZs
67 are, on average, growing and reducing their oxygen content [*Garcia et al.*, 1998; *Joos et*
68 *al.*, 2003; *Stramma et al.*, 2008a, 2009]. This trend has been related to global warming
69 and increased CO₂ levels [*Matear and Hirst*, 2003; *Oschlies et al.*, 2008], as well as to
70 natural decadal variability [*Gnanadesikan et al.*, 2007; *Deutsch et al.*, 2011], but the
71 exact ways how this is happening are yet to be deciphered. The key role of oxygen
72 content for the marine ecosystem endorses the crucial need for a better understanding of
73 the OMZs dynamics.

74
75 In this study we will focus on the North Atlantic OMZ (naOMZ) and how its water
76 mass is renewed. Earlier studies have assumed that most of the water supply to the
77 naOMZ comes from the south, through the cyclonic tropical circulation pattern
78 [*Stramma et al.*, 2005, 2008b; *Brandt et al.*, 2010, 2014], in agreement with the idea of
79 a shadow zone in the subtropical gyre [*Luyten et al.*, 1983] where the Cape Verde
80 frontal region acts as the barrier between the subtropical and the tropical gyres [*Fraga*,
81 1974, *Zenk et al.*, 1991]. The existence of an inter-hemispheric northward transfer of
82 mass linked to the upper limb of the Atlantic Meridional Overturning Circulation,
83 further leads to the predominance of southern origin waters in the whole tropical
84 thermocline [*Kirchner et al.*, 2009]. South Atlantic CW (SACW) and Antarctic IW

(AAIW) cross the equator mostly along the western margin via the North Brazil Current (NBC) and partly retroflect east to feed the tropical system of jets (Figure 1). The considered major pathways to the naOMZ are therefore subsurface eastward jets located south of 10°N: the North Intermediate CounterCurrent (NICC) at 2°N, the North Equatorial Undercurrent (NEUC) at 4°N, and the northern branch of the North Equatorial Countercurrent (nNECC) at 8-9°N [Stramma *et al.*, 2005; Karstensen *et al.*, 2008; Brandt *et al.*, 2010]. Nevertheless, the core of the naOMZ lies further north. The link between these jets and the naOMZ is therefore explained by the cyclonic circulation around the Guinea Dome, a general uplift of the isopycnals within the surface and subsurface levels driven by the local cyclonic wind-stress [Siedler *et al.*, 1992; Lázaro *et al.*, 2005]. Moreover, this northward branching to the naOMZ is enhanced along the African continent by the seasonal Mauritanian Current at the surface and by the ubiquitous subsurface along-slope Poleward Undercurrent [Barton, 1989; Mittelstaedt, 1991; Peña-Izquierdo *et al.*, 2012].

In addition to the advective supply, recent observational studies point out the notable role that meridional mesoscale stirring [Hahn *et al.*, 2014] and diapycnal diffusion play [Fischer *et al.*, 2013] in the local renewal of the naOMZ thermocline. These processes are especially relevant in the supply of oxygen due to the strong gradients, mostly meridional, observed in the oxygen field, which are related to the predominantly zonal circulation. However, it is the large-scale circulation that is the primary factor in settling the development of the naOMZ, while mixing leads to a homogenization of the hydrographic properties within. In this sense, while direct velocity observations and Lagrangian drifters show a clear connection between the NEUC/nNECC and the naOMZ at depths above 300 m [Stramma *et al.*, 2005, 2008b; Brandt *et al.*, 2010], neither observations nor numerical simulations [Elmoussaoui *et al.*, 2005] give evidence for a link at deeper levels. We may, therefore, wonder what is the maximum depth reached by this circulation scheme and what are the responsible dynamics further below.

Some hints to a vertical limit in the connection between the NEUC/nNECC and the naOMZ come from historical temperature and salinity profiles in the eastern tropical North Atlantic. A salinity and temperature inversion is usually observed at $\sigma_\theta = 26.8 \text{ kg m}^{-3}$ ($\sigma_{26.8}$), located at about 300 m within the CW stratum [Fraga, 1974; Voituriez and

118 *Chuchla*, 1978; *Poole and Tomczak*, 1999; *Pastor et al.*, 2012; *Peña-Izquierdo et al.*,
119 2012]. Fresher and colder waters are only found above this level, indicative of SACW,
120 while an enhanced influence of saltier and warmer North Atlantic CW (NACW) is
121 present below. *Voituriez and Chuchla* [1978] earlier proposed that this thermohaline
122 transition at $\sigma_{26.8}$ corresponds to a mean northward penetration of SACW in the
123 overlying layer and a southward inflow of NACW in the underlying layer. Nevertheless,
124 the circulation pattern leading to such a transition has not yet been properly addressed.

125
126 The numerical simulation of *Elmoussaoui et al.* [2005] shows that $\sigma_{26.8}$ roughly
127 matches with the deepest vertical extent of the northward branch of the nNECC heading
128 towards the naOMZ. Their results suggest that no direct water supply associated with
129 the NEUC/nNECC, and in turn with SACW, takes place below this level. Indeed,
130 oxygen concentrations decrease rapidly in the naOMZ below $\sigma_{26.8}$ [*Fischer et al.*,
131 2013], pointing to a weaker ventilation. The signal of NACW in this deep layer is
132 especially relevant because (1) it points to a new pathway and source of oxygen for the
133 naOMZ, not previously taken into account, and (2) simultaneously reveals a vertical
134 limit to the constraint for the equatorward transfer of mass from the subtropical gyre to
135 the shadow zone [*Luyten et al.*, 1983].

136
137 While other studies on the ventilation of OMZs have focused on the role played by the
138 tropical system of jets, in this study we investigate all the sources to the naOMZ CWs,
139 with particular emphasis on the northern subtropical gyre contribution. In order to
140 determine the geographical and vertical distribution of SACW and NACW, we first
141 carry out a water mass analysis for the whole tropical Atlantic from historical
142 observations. We then perform a numerical Lagrangian experiment to compute the
143 water mass pathways towards the naOMZ. The Lagrangian approach allows us to
144 consider the combined effect of mean flow, seasonal variability and mesoscale eddies -
145 incorporating the regional and mesoscale diapycnal advection - which have been
146 considered separately in earlier observational studies [*Stramma et al.*, 2005, 2008b;
147 *Brandt et al.*, 2010; *Hahn et al.*, 2014]. The joint analysis of the water mass distribution,
148 as deduced from observations, and the water mass composition, as deduced from the
149 Lagrangian pathways, provides independent but consistent views of the principal
150 processes leading to water mass renewal of the naOMZ.

151
152
153
154
155
156
157
158
159
160
161
162
163
164
165
166
167
168
169
170
171
172
173
174
175
176
177
178
179
180
181
182
183
184

2. Data and Methods

2.1 Dataset of T/S profiles

This work focuses on the northeastern tropical Atlantic Ocean but, as we are interested in the origin of the naOMZ water mass, the area of study spans the entire North Atlantic tropical Ocean (from 60°W to 0°) and from the southern hemisphere to beyond the southern edge of the North Atlantic Subtropical Gyre (from 5°S to 30°N). A dataset of observed temperature and salinity (*T/S*) profiles has been used, instead of a climatological database, to avoid the loss of variability after climatologic averaging. This dataset has been created with CTD profiles obtained from the National Oceanographic Data Center (<http://www.nodc.noaa.gov>) together with Argo profiles downloaded from the European Argo Data Center (<http://www.coriolis.eu.org>). While the set of CTD profiles used here spans a longer period of time (since 1971), their number is smaller than the number of available Argo profiles, which has been growing fast since 2005. Both Argo real time and delayed mode profiles have been included in this dataset. The initial data set includes 21,242 CTD casts and 39,919 Argo profiles, comprising data from 1971 to 2011. All *T/S* profiles are converted to the TEOS-10 formulation, i.e. conservative temperature and absolute salinity [Millero *et al.*, 2008].

Although the data centres perform an automatic quality control on the data, an additional procedure has been followed to ensure we have a high quality set of data: (1) For the CTD dataset, only profiles with an “accepted” NODC quality flag are used; (2) for the Argo dataset, only data with a “good” quality flag are selected; (3) profilers included in the grey list provided by the Argo data centres are removed; (4) all profiles are required to span the entire depth range between 100 m and 1000 m to ensure the sampling of the upper thermocline, with a minimum vertical resolution of 10 m for the whole profile; (5) all profiles with density inversions greater than 0.01 kg m⁻³ are removed.

After this initial selection, we retain a total of 9,607 CTD’s and 30,136 Argo *T/S*

185 profiles. The T/S values are then linearly interpolated to selected potential density
186 levels, on average separated by about 10 m. These interpolated profiles are then sorted
187 geographically in bins of $3.5^\circ \times 5^\circ$ degrees of latitude and longitude for a final statistical
188 test. The average T and S values at each density level are computed for each bin so that
189 any profile with data beyond three standard deviations from the mean is removed. The
190 final (T/S) dataset includes 30,485 profiles on σ_θ coordinates.

191

192 We also use the ocean oxygen content field from the annual WOCE atlas [*Gouretski and*
193 *Koltermann*, 2004] with 0.5° horizontal resolution and 45 vertical levels. An
194 advantageous feature of this climatology is the averaging on isopycnal levels, instead of
195 the more common isobaric computation. This method mimics the preferential along-
196 isopycnal mixing that occurs in the real ocean and therefore preserves the water mass
197 identities. For this same reason, throughout the whole manuscript we will use potential
198 density instead of depth coordinates.

199

200 *2.2 Water mass analysis*

201

202 A water mass analysis is carried out to distinguish the contribution of water masses with
203 southern and northern origin to the naOMZ thermocline. We focus on the CW stratum
204 where the upper part of the naOMZ is found; therefore, only the contributions of
205 NACW and SACW are calculated. We define these two water types as the mean T/S
206 profiles calculated between latitudes 5°S and 0°S for SACW, and between 25°N and
207 30°N for NACW, after averaging on isopycnal surfaces. The averaged profiles are
208 computed within the CW stratum, defined in the tropical Atlantic Ocean for σ_θ between
209 26.3 and 27.15 kg m^{-3} [*Kirchner et al.*, 2009]. Figure 2 shows how these definitions of
210 SACW and NACW correctly confine the variability of CWs within the tropical Atlantic.

211

212 The analysis here implemented is a simplified isopycnal version of the optimum
213 multiparameter analysis [*Mackas et al.*, 1987; *Tomczak and Large*, 1989]. The method
214 aims at finding the contribution of predefined water types to each data point, determined
215 as the best linear mixing combination in a multi-variable space. In our case we only use
216 two hydrographic variables (temperature and salinity) together with the mass
217 conservation constraint.

218

219 For every data point, each modeled variable $V_{Mod,i}$ (i.e. T/S and mass) is calculated from
 220 a combination of SACW and NACW proportions (x_{SACW} and x_{NACW}):
 221

$$V_{Mod,i} = x_{SACW}V_{SACW,i} + x_{NACW}V_{NACW,i}$$

222
 223 where $V_{SACW,i}$ and $V_{NACW,i}$ denote the values of the normalized variable i for the
 224 SACW and NACW water types at the density of the observation. For the conservation
 225 of mass ($i=mass$), the above equation becomes simply $V_{Mod,mass} = x_{SACW} + x_{NACW}$.
 226

227 The best combination is obtained minimizing, in a non-negative least squares sense, the
 228 total residual R , defined as
 229

$$\begin{aligned} R &= \sum_{i=T,S,mass} w_i r_i \equiv \sum_{i=T,S,mass} w_i (V_{Mod,i} - V_{Obs,i}) \\ &= \sum_{i=T,S,mass} w_i [(x_{SACW}V_{SACW,i} + x_{NACW}V_{NACW,i}) - V_{Obs,i}] \end{aligned}$$

230
 231 This total residual represents the weighed summation of the residuals of all three
 232 variables (r_i), each one calculated as the difference between the modeled ($V_{Mod,i}$) and
 233 observed ($V_{Obs,i}$) values. While T and S residuals are weighted equally ($w_T = w_S = 1$),
 234 mass conservation is enforced through a much a greater weight ($w_{mass} = 10$), therefore
 235 ensuring that the water sample is almost totally made from the combination of the
 236 predefined water types; note that $V_{Obs,mass} = 1$.
 237

238 2.3 The velocity field

239
 240 The numerical simulation used in this study is the open access product from the ECCO2
 241 project (Estimating the Circulation and Climate of the Ocean, phase II,
 242 <http://ecco2.jpl.nasa.gov>). The ECCO2 project synthesizes data obtained by least-
 243 squares fit of a global full-depth-ocean and sea-ice configuration of the Massachusetts
 244 Institute of Technology Ocean General Circulation Model [Marshall *et al.*, 1997]. It
 245 uses both satellite and in situ available data, including the CTD casts and Argo profiles
 246 described above. The simulation is an eddy-permitting solution with a $1/4^\circ$ horizontal

247 resolution and 50 vertical levels, spanning 20 years from 1992 to 2011 with a temporal
248 resolution of 3 days. The model, therefore, is capable of reproducing the largest
249 mesoscale features but cannot simulate the turbulence associated with scales smaller
250 than $1/4^\circ$. A comparison between satellite altimeter and the ECCO2 velocity fields [Fu,
251 2009] shows good agreement in the latitudinal variation of surface zonal velocities, a
252 reflection of the tropical system of zonal jets. A comparison between the water mass
253 distribution as calculated from hydrographic observations and the water mass
254 distribution deduced from the modeled Lagrangian pathways is discussed in section 4.
255 In section 5, the velocity fields from several observational studies are also compared
256 with the model velocity field.

257

258 We will use two different velocity fields to describe the processes that lead to the
259 thermohaline transition at $\sigma_{26.8}$. On a first and simplified case, we will use a fully
260 isopycnal two-dimensional (2D) field, computed by vertically averaging the original
261 ECCO2 horizontal velocities over 0.05 kg m^{-3} density layers. The Lagrangian advection
262 within this 2D field will always follow isopycnal surfaces and the vertical velocity is
263 therefore solely related to the isopycnals' slope. Second, we will use the original three-
264 dimensional (3D) ECCO2 velocity field. The comparison between both of these
265 velocity fields will allow us to distinguish between the isopycnal and diapycnal
266 components of the velocity in the ECCO2 product.

267

268 The vertical velocity field in ECCO2 does not capture small-scale processes like double
269 diffusion or turbulence related to vertical shear instabilities. Hence, in this work only
270 the contribution of regional scale and mesoscale diapycnal advection, as resolved by the
271 model, are taken into account for estimating the diapycnal component of the naOMZ
272 thermocline renewal (hereafter referred as diapycnal fluxes). We will take special
273 caution when interpreting these results because the vertical velocity in ECCO2 is
274 computed as a residual from the mass conservation condition in the horizontal plane.
275 ECCO2, as a depth-coordinate model, may have a preferential advection along z -
276 constant surfaces. Hence, in regions where the isopycnals are notably tilted, these
277 models may lead to an artificial diapycnal flux [Griffies *et al.*, 2000]. Nevertheless, as
278 shown by Figure 5 in section 4, this description appears to be accurate enough to
279 reproduce the water mass composition of the naOMZ thermocline.

280

281 On the other hand, the eddy-permitting, but not fully-resolving, ECCO2 velocity field
282 may underestimate the strength of the tropical system of jets and the horizontal
283 turbulent diffusion. *Duteil et al.* [2014] have shown that the model horizontal resolution,
284 i.e. the model ability to resolve mesoscale structures, plays a major role in reproducing
285 the thermocline oxygen content of the tropical Atlantic. Although we focus on the water
286 mass distribution rather than oxygen content, in order to compensate for this
287 underestimation of small-scale dispersion, sub-grid diffusion will be artificially added in
288 the computation of the Lagrangian trajectories as proposed by *Döös et al.* [2011] and
289 briefly summarized below.

290

291 2.4 The Lagrangian experiment

292

293 Lagrangian trajectories are computed using the Connectivity Modeling System version
294 1.1 (CMS) [*Paris et al.*, 2013] that tracks virtual particles within a numerical circulation
295 model. An advantage of the CMS package is that it allows adding artificial eddy
296 diffusivity to simulate dynamics with a smaller spatial scale than the model grid
297 resolution. This artificial turbulence is here parameterized by including a stochastic
298 impulse (I) each time-step particles are advected. As in *Döös et al.* [2011], this impulse
299 consists of an extra horizontal velocity parameterized according to $I = r \sqrt{2K/dt}$,
300 where K is the horizontal eddy diffusivity coefficient, dt is the time step, and r is a
301 random number between -1 and 1 from a Gaussian distribution. In our case, with a $1/4^\circ$
302 horizontal resolution model, we tested $K = 0, 50, 100$ and $1000 \text{ m}^2 \text{ s}^{-1}$, and the best fit
303 to observations (section 4.1) corresponded to using $K = 100 \text{ m}^2 \text{ s}^{-1}$ together with the
304 original 3D velocity field. This value is in reasonable agreement with *Döös et al.*,
305 [2011] who obtained $K = 300 \text{ m}^2 \text{ s}^{-1}$ as the best fit between the dispersion of real ocean
306 surface drifters and virtual particles within a $1/4^\circ$ resolution model. The focus on
307 subsurface levels in our study likely explains the smaller values we use for K .

308

309 In order to discern the role that diapycnal fluxes and the horizontal subgrid-scale
310 diffusion play in the water mass renewal of the naOMZ, we will use four different
311 Lagrangian simulations of increased complexity, corresponding to the 2D and 3D
312 velocity fields with and without a subgrid scale diffusion of $K = 100 \text{ m}^2 \text{ s}^{-1}$ (section 4).

Specifically, we will compare the outcomes from the following four simulations: 2D isopycnal velocity field without subgrid-scale diffusion (ISO-K0); 2D isopycnal velocity field adding subgrid-scale diffusion (ISO-K100); original ECCO2 3D velocity field with no added diffusion (3D-K0); and the 3D velocity field with added subgrid-scale diffusion (3D-K100). In particular, the contribution of the diapycnal fluxes to the water supply will be assessed by comparing the ISO-K100 and 3D-K100 simulations.

As we are interested in the source of the naOMZ waters, we release particles within the naOMZ and advect them backwards in time for up to 100 years. This means that we are computing all trajectories that end up in the naOMZ in a realistic forward time simulation. In order to attain a time series 100 years long, the available 20-year numerical simulation is therefore looped in the same way as in *van Sebille et al.* [2012, 2013]. The release region for the virtual particles, hereafter defined as the naOMZ box, is located between 9°N and 17°N and east of 22°W (Figure 1). This box roughly comprises the climatological vertically-averaged contour of $60 \mu\text{mol kg}^{-1}$ for oxygen content within the 200-500 m depth layer while it also includes the region where most of the lowest oxygen values have been recently located [*Fischer et al.*, 2013] at the core of the naOMZ. In each experiment, a total of 170,000 virtual particles are randomly seeded every 15 days during the first 5 years of the simulation. For simplicity, although the Lagrangian simulation is computed backwards in time from the naOMZ box, in the manuscript we will always describe particle trajectories in a realistic forward time, always ending in the naOMZ.

The vertical extension of this study covers the CW stratum with the aim of discerning the distinct circulation patterns at depth that lead to the thermohaline transition observed at the $\sigma_{\theta} 26.8$ density level. Following previous studies in the tropical Atlantic [*Elmoussaoui et al.*, 2005; *Rhein et al.*, 2005; *Kirchner et al.*, 2009; *Peña-Izquierdo et al.*, 2012] we will refer to waters with σ_{θ} between 26.3 and 26.8 kg m^{-3} as the upper CW (uCW) and to waters with σ_{θ} between 26.8 and 27.15 kg m^{-3} as the lower CW (lCW).

3. Water mass of the naOMZ

346

347 Hydrographic observations in the northeastern tropical Atlantic Ocean show an abrupt
348 thermohaline transition usually centered at $\sigma_{26.8}$ [Voituriez and Chuchla, 1978]. For
349 any T/S diagram in this region, the transition can be easily detected within the CW
350 stratum as a marked salinity depth inversion, sometimes also present in temperature,
351 indicative of a change in the water mass composition. A relatively fresh and cold water
352 mass indicates the presence of SACW in the uCW while the salty and warm water
353 suggests a greater influence of NACW in the ICW. Figure 3 shows this transition as
354 characteristic for the whole northeastern tropical Atlantic, being clearly present as far
355 west as 40°W and as far south as 7°N. In general, the salinity inversion becomes
356 stronger and shallower moving northeastward in the tropical North Atlantic.

357

358 This transition is also found in the model climatological mean, with a similar
359 geographic pattern and at the same levels as in the observations (Figures 3a and b). The
360 main difference is observed near Africa at 20°N where observations show a region with
361 T/S transition profiles at density levels shallower than observed in the model. This
362 difference is likely due to temporary NACW and SACW interleaving in the frontal zone
363 related with eddies or filaments [Tomczak, 1981], and are not properly represented by
364 the model climatology that only includes permanent features. Therefore, this ubiquitous
365 hydrographic footprint suggests a permanent and distinct circulation pattern between the
366 uCW and the ICW. Moreover, the vertical distribution of fresher and colder SACW
367 above saltier and warmer NACW avoids the development of salt fingering thus
368 favouring the permanence of this feature in time.

369

370 A simple explanation for the formation of the thermohaline transition arises from the
371 spatial distribution of the T/S diagrams (Figure 3). Zone A corresponds to the NEUC
372 and nNECC region. The T/S diagrams in the naOMZ (zones B and C) indicate the
373 presence within the uCW of pure southern waters advected by these jets, thus revealing
374 a direct connection with zone A. However, the lack of these southern waters in the ICW
375 suggests this connection disappears below $\sigma_{26.8}$, particularly in the northern area (zone
376 C).

377

378 The water mass analysis helps us understand the exact contribution of southern and

379 northern water masses in the renewal of the tropical North Atlantic upper thermocline
380 (Figure 4). The distributions of NACW and SACW exhibit opposite patterns above and
381 below $\sigma_{26.8}$. In the uCW, SACW stretches north along the eastern margin while
382 NACW penetrates into the tropical Atlantic from the western margin. This pattern
383 agrees with the circulation scheme proposed by *Schott et al.* [2008] for the subtropical
384 cell, with an intense northward flow along the eastern margin, especially in autumn
385 [*Elmoussai et al.*, 2005]. In contrast, in the ICW, SACW is advected along the
386 American continent towards the Caribbean Sea while NACW spans southwards along
387 the African coast. A similar pattern was suggested by *Poole and Tomczak* [1999] from
388 data before the Argo era, with much lower horizontal resolution. In summary, the
389 naOMZ is dominated by SACW in the uCW while an equally split mixture of NACW
390 and SACW is found in the ICW .

391
392 The presence of a large fraction of NACW in the ICW is very relevant for the oxygen
393 supply to the naOMZ since NACW is more recently ventilated than SACW, thus having
394 higher oxygen content. Nevertheless, the mean patterns for regions B and C (Figure 4)
395 show that the oxygen concentration decreases just below $\sigma_{26.8}$, where the NACW
396 proportion notably increases; in particular, the absolute oxygen minimum is found at
397 $\sigma_{27.1}$, exactly where the NACW fraction is largest. Further, for the ICW, the proportion
398 of NACW is quite homogeneous within the naOMZ, as shown by the local minimum in
399 the standard deviation of this fraction (Figure 4d). The presence in this region of a well-
400 mixed water mass, with a notable contribution of NACW but minimal oxygen content,
401 can be explained by a marked reduction in the water renewal rate within this layer.
402 These results agree with the existence of a regional water mass variety for the naOMZ
403 (the Cape Verde SACW, i.e. SACWcv), as proposed by *Peña-Izquierdo et al.* [2012].
404 Such regional water mass would explain the presence of two bands of relatively high
405 standard deviations in the eastern Atlantic, south of 10°N and north of 15°N,
406 representative of two different mixing regions: SACW with SACWcv to the south, and
407 SACWcv with NACW to the north (Figure 4d). Therefore, for the ICW, both SACW
408 and NACW would reach the naOMZ while slowly mixing with SACWcv, therefore
409 reducing the oxygen content.

410

411 These observations lead to two main questions: What are the water mass pathways that

412 lead to such a vertical water mass distribution? And what role does NACW play in the
413 ventilation of the naOMZ? In the following two sections we will answer these questions
414 with the help of the backward Lagrangian experiments, computing the pathways
415 followed by the water masses that end in the naOMZ at different density levels.

416

417

418 **4. Lagrangian simulations**

419

420 The contributions of the different water masses that make up certain regions of the
421 ocean can also be inferred from the trajectories of the water parcels, or Lagrangian
422 particles, that end up in that region. Specifically, the analysis of the origin of all
423 particles ending in the naOMZ should be comparable with the water mass analysis
424 carried out in section 3. Both analyses should independently lead to similar water mass
425 contributions to the naOMZ. A good agreement among them should be considered as a
426 consistent validation of the ocean model velocity fields and the inferred Lagrangian
427 trajectories.

428

429 *4.1 Lagrangian stream function*

430

431 One way to reveal the average pattern of a set of trajectories is to compute a Lagrangian
432 stream function (LSF). Analogous to the standard (Eulerian) stream function, which
433 accounts for the flux between neighbouring points at any given time, the LSF accounts
434 for the net number of particles (or trajectories) that flow between two grid points
435 throughout the entire simulation. However, it is important to note that the LSF does not
436 show the average circulation within a region, as the Eulerian stream function does.
437 Instead, it represents the average pathways followed by a selected set of particles, that
438 may be named conditional pathways. Thus, the LSF only shows a subset of the
439 circulation, in our case, the pathways to the naOMZ.

440

441 To compute a stream function, the flow should always be non-divergent. In the case of a
442 LSF, this means that trajectories should start and end out of the domain. The summation
443 of the latitudinally flowing particles is carried out along parallels, moving east from the
444 western boundary and considering as positive (negative) counts those particles that
445 move north (south), i.e. particles always flow with larger LSF values to the right. We

446 have also taken the zero LSF reference value at the south-western grid point of the
447 domain. These definitions imply that the sign of the LSF is related to the origin of the
448 trajectories; positive (negative) values are related with southern (northern) origin
449 particles. Finally, the LSF values are normalized by the total number of particles, so
450 they represent the proportion of particles that follow a specific pathway. For further
451 details about the LSF computation, the reader is referred to *Blanke et al.* [1999] or *Döös*
452 *et al.* [2008].

453

454 In section 3 we have shown that the thermohaline transition observed at $\sigma_{26.8}$ is a
455 permanent feature of the northeastern tropical Atlantic. Such a marked and persistent
456 hydrographic footprint requires a continuous generating mechanism. We suggest that
457 the uCW and ICW should be governed by different dynamics leading to a continuous
458 supply of distinct water masses in each layer. However, diffusive processes, especially
459 diapycnal fluxes, should counteract this differentiation. To distinguish between
460 developing and erasing processes, we use the following three Lagrangian simulations:
461 isopycnal velocity field and no added subgrid-scale diffusion (ISO-K0), 3D velocities
462 but no added subgrid-scale diffusion (3D-K0), and 3D velocities with added horizontal
463 subgrid-diffusion (3D-K100) (section 2.4).

464

465 Figure 5 compares, for all three simulations, the mean vertical profile of the observed
466 proportion of NACW within the naOMZ (black line) with the proportion of particles
467 having a northern origin (coloured lines). Note that in order to show the Lagrangian
468 pathways within the tropical Atlantic, the LSF is computed between 5°S and 30°N. This
469 implies that particles of southern and northern origin respectively come from south of
470 5°S and north of 30°N. This criterion is potentially too restrictive, as SACW contributes
471 over 80% south of 6°N, and NACW contributes more than 80% north of 20°N (Figure
472 4). Therefore, we could alternatively assign a SACW fingerprint to those particles
473 arriving to the naOMZ from south of 6°N, and a NACW signature to those particles
474 arriving from north of 20°N. Hereafter, we will distinguish between particles arriving
475 from south/north of 6°N/20°N and the more restrictive definition of particles of
476 southern/northern (5°S/30°N) origin. Notice that, with the less restrictive definition
477 (6°N/20°N), a trajectory starting south of 5°S but flowing between 20°N and 30°N
478 before entering into the naOMZ will be considered as a 20°N particle despite its
479 southern origin. For comparison, Figure 5 shows the profiles following both criteria in

each simulation. The two profiles agree in general although, as expected, the 6°N/20°N is closer to the observations for all simulations.

4.2 Water mass pathways: ISO-K0

The contribution of northern particles increases markedly with depth near $\sigma_{26.8}$ for all simulations, in agreement with observations. However, the transition in the vertical profile is especially abrupt in the isopycnal simulation (ISO-K0, Figure 5a), with a roughly constant 10% contribution of 20°N particles above $\sigma_{26.8}$ but increasing largely just below, reaching 63% at $\sigma_{27.1}$. This unrealistic abrupt transition between the uCW and lCW is likely due to the neglect of diapycnal fluxes. Nevertheless, this also points to the distinct dynamics that rule the isopycnal circulation in each layer.

The LSF shows clearly different patterns between the uCW and lCW for the ISO-K0 case (Figures 6a and b). For the uCW, the major (above 80%) contribution of southern origin particles (red shading) is displayed via a continuous and successive northward branching from the tropical system of jets toward the naOMZ, throughout the whole zonal basin extension. Most of these particles cross the equator along the American continent via the NBC and then retroflect east to feed the EUC at 0°N and the NEUC at 4°N. East of 40°W, northward branching of these jets joins the nNECC flow at about 8°N. Similarly, the nNECC successively branches as it moves north, before entering the naOMZ mostly within a broad latitudinal band between 10°N and the Cape Verde Islands. Northern origin particles (blue contours) within this layer enter the tropics mainly through the western margin, retroflecting east from the southwestward subtropical gyre flow, in agreement with observational studies [Kirchner *et al.*, 2009]. However, the contribution of northern origin particles is overestimated (Figure 5a) likely as a result of the inability of the isopycnal simulation to properly reproduce the outcropping of the lighter isopycnals north of 20°N.

For the lCW (Figure 6b), the LSF computed from the ISO-K0 simulation displays three main differences in comparison with the uCW. The first difference, as previously shown in Figure 5a, is the notable contribution of northern origin particles. They retroflect eastwards south of 20°N, just north of the Cape Verde Islands, from the main

513 southwestward flow of the eastern boundary current and eventually reach the naOMZ,
514 directly from this zonal current or after recirculating south along the continental slope.
515 The second difference is the main pathway followed by southern origin particles. They
516 enter into the tropical North Atlantic also via the NBC and retroflect to directly feed the
517 nNECC at about 8°N. Virtually all southern origin particles leave the nNECC before
518 30°W, branching north into a progressively narrowing band of eastward flow. This
519 occurs just south of 15°N, in what appears to be the main conduit of southern origin
520 particles to the naOMZ in this lower layer. The simulation reveals that, within the ICW
521 and in contrast with the uCW, there is essentially no pathway from the tropics to the
522 naOMZ east of 30°W and south of 10°N.

523

524 Finally, the third difference between the uCW and ICW pathways relates to their time
525 scales. Figures 7a and 7b (blue lines) display the average time (in years) required by
526 particles to reach the naOMZ box from any point of the domain. For example, we can
527 compare the regions where southern and northern origin particles enter into the tropical
528 North Atlantic, via the NBC across the equator and via the southwestward flow of the
529 NEC between 20°N and 25°N, respectively. No matter the origin, the times are similar
530 within a layer: between 10 and 15 years for the uCW and between 40 and 50 years for
531 the ICW. The isopycnal simulation suggests that the time scale is 3-4 times longer in the
532 ICW than in the uCW. The advection times show, for the ICW, a notable disconnection
533 between the naOMZ and the region lying just south, with transit times over 50 years for
534 a distance shorter than 3° of latitude (Figure 7b).

535

536 *4.3 Water mass pathways: 3D-K0*

537

538 When Lagrangian particles are allowed to change their density level along their
539 trajectory (3D-K0), the abrupt vertical transition between the uCW and the ICW is
540 greatly smoothed (Figure 5b). The exchange of particles between different density
541 levels leads to a homogenization in the water mass supply of the naOMZ. Some of the
542 particles originally at less dense levels, thus of a predominant southern origin, will
543 finally end within the naOMZ at more dense levels, explaining the reduction of northern
544 particles in the ICW. This feature is also noticeable in the LSF of the ICW layer (Figure
545 6d): the pathways followed by the particles ending in the ICW of the naOMZ now
546 resemble those followed by the uCW particles. In this simulation, roughly 30% of all

ICW particles reach the naOMZ directly from the nNECC (south of 10°N) or from even further south. This circulation is very different from the isopycnal simulation (Figure 6b) where this pathway is totally absent. Additionally, the advection times within the ICW are reduced by about 25% (Figure 7d). In contrast, the contribution to the uCW of northern particles is still minimal, i.e. no transfer from deeper levels is observed. Consistently, the general scheme of the LSF and the advection times for uCW are only slightly modified with respect to the ISO-K0 simulation. This asymmetry in the vertical transfer of particles between the two layers will be detailed in section 4.5.

On the other hand, the diapycnal fluxes in the 3D-K0 simulation underestimate the contribution of the northern particles, especially in the ICW. This suggests there may be other processes playing an important role in the water mass renewal of the naOMZ. The next section addresses this question.

4.4 Water mass pathways: 3D-K100

Mesoscale dynamics may play a major role in the renewal of the OMZ thermocline [Duteil *et al.*, 2014; Hahn *et al.*, 2014]. Since the eddy-permitting ECCO2 model does not fully resolve those processes responsible for the generation of mesoscale eddies, the ventilation of the naOMZ may be underestimated (Figure 5b). For this reason, in our Lagrangian approach, the effect of the unresolved eddies is simulated by adding horizontal subgrid-scale diffusion to the model trajectories (3D-K100 simulation, see Methods).

The added horizontal diffusion enhances the proportion of northern particles, so that it becomes remarkably similar to the observational profile (Figure 5c). This added diffusion has two main effects. First, it leads to a substantial increase in the water transfer from the northern subtropical gyre across the frontal zone, particularly in the ICW where the main flow is sluggish. The added diffusion increases the number of northern origin particles leaving the subtropical gyre and entering the naOMZ via the eastward flow just south of 20°N (Figure 6f), as also seen in the ISO-K0 simulation. The second effect is to strengthen the northward transfer from the NEUC and nNECC. As a consequence, the advection times (Figures 7e and 7f) from the subtropical gyre and the north equatorial jets into the naOMZ are reduced (20-30%) compared with the two

581 previous simulations. This is especially relevant for the supply of oxygen, as it implies
582 an enhanced connection from these more oxygenated regions (Figure 1) and thus a more
583 efficient ventilation of the naOMZ.

584
585 For the 3D-K100 simulation, a more detailed description of the water supply to the
586 naOMZ is presented in Figure 8. It shows the inflow of particles across a control section
587 located 3° outside the naOMZ box, where particles are released, distinguishing the
588 preferential pathways into the naOMZ. Since particles may cross this control section
589 several times, we only show where and when they cross it for the last time before
590 reaching the naOMZ box. The results of the 3D-K100 simulation may also be used to
591 calculate the fraction of NACW that enters the naOMZ box at different levels. This
592 supply is calculated as the observational proportion of NACW at the location where
593 each particle enters the box, and then adding the contributions for all arriving particles.
594 The profile of this NACW supply (green line in Figure 5) fits the observations
595 remarkably well in all simulations, although becomes progressively better as we
596 introduce diapycnal fluxes and added diffusion. The goodness of this agreement, which
597 depends on both the particle pathways and the NACW content at the location where the
598 particles enter the box, grants further confidence to the model velocity field, i.e. if the
599 entry pathways were incorrect then the NACW supply would differ from the proportion
600 of NACW observed within the naOMZ box.

601
602 Several inflows are clearly distinguished in Figure 8 and their contribution to the total
603 supply is summarized in Table 1. Within the uCW, the shallow northward NEUC branch
604 and the direct inflow of the nNECC are the major contributors (56%), with only a minor
605 inflow arriving north of the Cape Verde Islands (5%). For the ICW, the water supply is
606 more northerly: the combined contribution of the NEUC and nNECC is halved (28%), a
607 pronounced maximum inflow is found centred at 14°N (29%), and the inflow north of
608 the Cape Verde Islands is doubled (30%). At the core of the naOMZ ($\sigma_{27.1}$), a major
609 contributor (27%) is the northward flow arriving from south of 6°N; since the ISO-K0
610 simulation shows a negligible inflow south of 6°N, the conclusion is that this inflow is
611 primarily driven by diapycnal fluxes and enhanced eddy diffusion. Nevertheless, the
612 zonal flow north of the Cape Verde Islands contributes one third of the total water
613 supply to the naOMZ, in remarkable contrast with the importance traditionally assigned

614 to the southern pathways (NICC and nNECC). Moreover, it is noteworthy that the
615 contribution of 20°N particles reaches up to 45% at $\sigma_{27.1}$ (Figure 5c); this is a
616 substantial increase compared with the other simulations, yet less than the 50%
617 observed fraction of NACW (Figure 3), thus the supply from the northern subtropical
618 gyre at this level is still slightly underestimated in this simulation. Additionally, the
619 mean advection times for arrival from the control section to the naOMZ box (Figure 8d)
620 are much shorter for the northern pathways than for the southern ones.

621

622 *4.5 Diapycnal component*

623

624 The changes in the pathways from the ISO-K0 to the 3D-K0 simulations indicate a
625 remarkable role of the meso- and regional-scale diapycnal advection in the renewal and
626 vertical redistribution of the naOMZ water mass, especially within the ICW. To
627 understand why this occurs, we look at the evolution of the density distribution of
628 particles ending at several density levels within the naOMZ (Figure 9). The density
629 distributions are Gaussian-like, approximately centered around the ending density level
630 as expected for isotropic vertical mixing arising from small-scale processes (double
631 diffusion and shear-induced). However, for some destination levels, there are significant
632 net upward or downward deformations (Figure 9a). Particles ending in the upper levels
633 of the naOMZ, above $\sigma_{26.7}$, come mainly from higher densities thus pointing to
634 upward diapycnal velocities (Figure 9b). Conversely, below $\sigma_{26.7}$, particles mostly
635 have a lighter density origin, i.e. downward diapycnal velocities. These contrasting
636 vertical motions within the uCW and ICW contributes to the distinct horizontal patterns
637 for these two layers, as shown in the previous sections.

638

639 Nonetheless, these vertical motions should be taken with caution since, as noted in
640 section 2, z-coordinate models as ECCO2 may induce spurious diapycnal diffusion
641 especially in those levels where the isopycnals are more vertically slanted, such as in the
642 upper levels. In order to verify whether the diapycnal processes leading to the
643 distributions are within realistic values, we compare the vertical dispersion of our
644 numerical particles (Figure 9) with the GUTRE tracer experiment in the naOMZ
645 [Banyte *et al.*, 2012]. On one hand, we look at the shape of the vertical distribution after
646 the first year of the backward simulation (dotted lines in Figure 9) that is quite

647 symmetric and accurately resembles quantitatively the Gaussian distributions observed
 648 in *Banyte et al.* [2012] for the first two years after the tracer release. On the other hand,
 649 we estimate the mean diapycnal velocity as the temporal rate of change in the average
 650 density of a subset of particles ending at a certain density level (Figure 9b); we assign
 651 this average density to the median of the density distribution at a given time. The mean
 652 diapycnal velocities calculated in this way range between $+4.1 \times 10^{-10} \text{ kg m}^{-3} \text{ s}^{-1}$ in the
 653 upper levels and $-1.8 \times 10^{-10} \text{ kg m}^{-3} \text{ s}^{-1}$ in the lower levels. The average diapycnal
 654 velocity obtained by *Banyte et al.* [2012] at $\sigma_{26.9}$ was $+1.5 \pm 2.7 \times 10^{-10} \text{ kg m}^{-3} \text{ s}^{-1}$,
 655 slightly smaller but of the same order of magnitude as our estimates. These results grant
 656 us confidence on the realism of the numerical simulation, indicating that the diapycnal
 657 fluxes deduced from the Lagrangian experiment are not grossly biased by spurious
 658 diapycnal diffusion. The estimated net diapycnal flux can thus be attributed to a real
 659 regional-scale process that is reasonably well reproduced in the ECCO2 model.

660
 661 The exchange of particles between distinct density levels (Figure 9) points out that
 662 diapycnal fluxes should have an impact on the naOMZ renewal times, as different levels
 663 have different advection times (Figure 7). We can quantify the contribution of this
 664 diapycnal component in the renewal of the naOMZ water mass by comparing the
 665 Lagrangian simulations with and without diapycnal fluxes (3D-K100 and ISO-K100).
 666 The only difference between the two outcomes will respond to meso- and regional-scale
 667 diapycnal fluxes. A first step is computing the function, $n(t)$, that counts the amount of
 668 particles within the naOMZ as a function of time, thereby identifying the time scales of
 669 water mass renewal (Figure 10a). When this function reaches 100%, the naOMZ is
 670 completely renewed, full of particles; this moment corresponds to the beginning of the
 671 backward simulation. From this function, inferring the renewal times, i.e. the required
 672 time to renew a certain percentage of the whole naOMZ water mass, is straightforward
 673 (Figure 10b). The inflow of particles towards the naOMZ is given by the change of $n(t)$
 674 in time, $F(t) = dn/dt$. We may then compute the purely isopycnal inflow, $F_{iso}(t)$,
 675 obtained from the ISO-K100 simulation and the isopycnal+diapycnal inflow, $F_{3D}(t)$,
 676 from the 3D-K100 experiment. The effect of diapycnal fluxes in the water mass renewal
 677 of the naOMZ is quantified as $f_{dia}(t) = F_{dia}/F_{3D} = (F_{3D} - F_{iso})/F_{3D}$.

678
 679 Figure 10c shows the average vertical profile of f_{dia} . Below $\sigma_{26.7}$, f_{dia} is positive

680 because a large proportion of particles ending at these levels come originally from
681 lighter and swifter levels (Figure 9b). As a consequence of this prevailing downwelling,
682 the water supply to the naOMZ is enhanced about 10-20% within the ICW. On the other
683 hand and within most of the uCW, the predominant upwelling leads to a 10%
684 weakening of the water mass renewal.

685

686

687 **5. The upper thermocline circulation in the ECCO2 model**

688

689 *5.1. The northeastern tropical Atlantic*

690

691 We may now connect the features that have emerged from the Lagrangian analysis with
692 the general circulation of the northeastern tropical Atlantic as deduced from the model.
693 We start by investigating the Eulerian layer-averaged velocity fields. In the uCW, the
694 model shows a broad cyclonic pattern dominating the annual mean circulation (Figure
695 11a). The mean eastward flow south of the Cape Verde Islands carries water from the
696 tropical to the subtropical regions through a marked northward detour between 30°W
697 and the African continent. This flow is especially enhanced along the continental slope
698 by the PUC, associated with the coastal upwelling system [Barton, 1989; Mittelstaedt,
699 1991; Peña-Izquierdo *et al.*, 2012]. Similar results arise from the numerical simulation
700 of El moussaoui *et al.* [2005], with a maximum northward transport (including now the
701 uCW and the surface layer) of 4Sv during boreal fall. After joining the westward flow
702 of the subtropical gyre, some of this water recirculates south towards the tropics and
703 then eastwards again via the nNECC and NEUC [Fratantoni *et al.*, 2000].

704

705 The cyclonic tropical path forms part of a complex basin-wide recirculation scheme that
706 also includes upwelling along the eastern tropical edge and subduction along the
707 southeastern subtropical gyre boundary, the so called subtropical cell (STC) [Zhang *et al.*, 2003; Schott *et al.*, 2004; Hazeleger and Drijfhout, 2006]. Further evidence of this
708 pattern can be found in the mean vertical velocity (Figure 11c). As previously revealed
709 from the Lagrangian trajectories, the uCW of the naOMZ is influenced by upwelling,
710 largely enhanced near the continental slope likely due to the coastal upwelling system.
711 North of the Cape Verde Islands, a predominant downward velocity is found related to
712 the subtropical gyre subduction. It is also important to distinguish the Guinea Dome
713

714 from the STC, the former being a much smaller-scale system acting at shallower levels,
715 located further south and directly driven by the regional cyclonic wind stress [*Siedler et*
716 *al.*, 1992; *Lázaro et al.*, 2005].

717

718 In the ICW, the mean velocity field is relatively weak, with circulation patterns less
719 defined than in the uCW (Figure 11b), yet two main structures can be detected. The first
720 one is an anticyclonic gyre located south of the Cape Verde Islands, made up of a well-
721 defined eastward flow at 14°N, all the way from at least 35°W to the African continent,
722 and a southwestward recirculation reaching as far south as 10°N. This pattern therefore
723 weakens the direct penetration to the naOMZ of water from the south. A similar
724 anticyclonic circulation, as deduced from geostrophic calculations, was proposed by
725 *Reid* [1994] for the AAIW layer, located below $\sigma_{27.15}$. The southward extension of the
726 contour with 20% content of NACW (Figure 11b) corroborates that this gyre reaches the
727 CW stratum. Furthermore, the existence of a relatively closed anticyclonic circulation
728 also agrees with the observed standard deviation minimum in NACW proportion
729 (Figure 4d), indicating the presence of a well mixed water mass, the previously
730 mentioned SACW_{cv} [*Peña-Izquierdo et al.*, 2012].

731

732 The second ICW structure is the cyclonic recirculation of part of the subtropical waters
733 (with high proportion of NACW) via a predominant eastward flow centred at 18°N. Part
734 of the water recirculates northward but some joins the southern anticyclonic gyre
735 through a southward flow along the slope, south of 18°N. Recent velocity observations
736 during the fall season along the African continental margin [*Peña-Izquierdo et al.*, 2012]
737 have shown a similar circulation pattern for the uCW and ICW layers. They suggest a
738 convergent meridional flow at 22°N in the uCW and divergent at 18°N in the ICW.
739 Thus, south of 18°N the continental slope current system is made up by an intense PUC
740 in the uCW and an enhanced southward flow in the ICW, in agreement with the model
741 velocity field. The mean vertical velocity within the ICW (Figure 11d) also displays a
742 contrasted pattern with respect to the uCW: predominant downwelling/upwelling taking
743 place south/north of the Cape Verde Islands.

744

745 The opposite horizontal and vertical patterns in the uCW and ICW strata resemble the
746 scheme of stacked meridional overturning cells proposed by *Wang* [2005] for both sides

747 of the equator. The upper cell, the so called tropical cell [Lu *et al.*, 1998] occupies the
 748 upper 100 m and is made up by the equatorial Ekman-driven upwelling, surface
 749 poleward flow until the downwelling band at 3°-4° of latitude, and equatorward flow at
 750 the subsurface. The lower cell, named the sub-thermocline tropical cell [Wang, 2005],
 751 has a weak circulation between 100 and 300m, with a pattern opposite to the tropical
 752 cell. Analogously, we propose for the northern part of the tropical Atlantic, and for
 753 larger spatial and temporal scales, a very simplified arrangement of stacked meridional
 754 overturning cells within the uCW and lCW. The upper cell (Figure 11e) would
 755 correspond to the subtropical cell while the lower one (Figure 11f) would respond to a
 756 lower subtropical cell with reversed flow direction. No direct observations of the whole
 757 system are available, yet the simplified layered circulation model discussed by
 758 Fratantoni *et al.* [2000] also appears to capture the opposing vertical velocity fields that
 759 correspond to the opposing cells (their Figure 15).

760
 761 While a detailed understanding of the processes that lead to such a complex three-
 762 dimensional circulation is beyond the scope of this work, we may look for some hints in
 763 the structure of the thermocline. The distributions of the depth and thickness of the
 764 uCW and lCW (Figure 12) suggest the existence of a baroclinic mode of circulation:
 765 those regions with a relatively thick uCW layer have a correspondingly thin lCW layer
 766 and vice versa. The similarity between the observed circulation patterns and the bottom
 767 depth of each layer suggests that the flow might be approximately represented with a
 768 3.5 layer geostrophic model (three active layers and a quiescent fourth layer; see e.g.
 769 section 4.1 in Xuang [2010]). The surface layer would correspond to the layer directly
 770 driven by Ekman pumping. The second and third layers would correspond to the uCW
 771 and lCW layers and the fourth layer, formed by deeper waters, would be passive. Let us
 772 call z_u and z_l the depths where we find the bottom of the uCW and lCW layers.
 773 According to this simple geostrophic layered model, the stream function for the third
 774 layer (lCW) would roughly match with the contours of constant z_l (Figures 11b and
 775 12b), and the streamlines for the second layer (uCW) would follow contours of constant
 776 $z_u + z_l$; since the horizontal gradients of z_u are substantially larger than those for z_l , this
 777 means that the stream lines in the second layer will approximately follow the contours
 778 of constant z_u (Figures 11a and 12a). Therefore, the circulation patterns in the uCW and
 779 lCW layers display opposite directions, as expected for a baroclinic mode of oscillation
 780 in a layered ocean.

781

782 A complementary explanation for these distinct patterns comes from requirements of
783 potential vorticity (PV) conservation by water parcels (Figures 12e and f). The
784 predominant stretching of the uCW in the naOMZ region limits the transfer of water
785 from the subtropical gyre. In order to preserve the PV, a southward displacement of a
786 water parcel, thus a stretching, should be balanced by an increase in its planetary
787 vorticity, i.e. a northward displacement. This is the principle for the existence of the
788 shadow zone in the classical theory of the thermocline ventilation [Luyten *et al.*, 1983].
789 However, the opposite situation occurs in the ICW: the thinning of this stratum favours
790 the existence of a southward flow, manifested by the southward deformation of the PV
791 contours and revealing a water transfer from the subtropical gyre within the ICW.

792

793 5.2 The Cape Verde Current System

794

795 Our analysis on the renewal of the naOMZ relies largely on how realistic the ECCO2
796 velocity field is. Support comes from the good agreement between the water mass
797 distribution within the naOMZ deduced from observations and from the simulated
798 Lagrangian pathways (Figure 5). For further validation, we now proceed to compare the
799 annually-averaged ECCO2 field along a meridional section at 25°W with previous
800 observational studies.

801

802 The pathways displayed in Figure 6 are evidence of the characteristic zigzag circulation
803 pattern within the tropical ocean, with a net eastward motion (NEUC at 4°N and
804 nNECC at 8-9°N). Our results also reveal the prevalence of other eastward currents
805 reaching as far north as 18°N, playing a remarkable (and not yet properly
806 acknowledged) role in the water supply to the naOMZ (Figure 8 and Table 1). The most
807 notable of these inflows is found at 14°N, clearly identified in ECCO2 down to 800 m
808 (Figure 13a). These modelled currents agree well with the velocity fields as determined
809 from several observational studies for the CW stratum in this area. Acoustic Doppler
810 Current Profiler (ADCP) observations along 23°W in July 2006 [Stramma *et al.*, 2008b]
811 show an intense eastward current at 14°N, reaching 20 cm s⁻¹ in the uCW and 10 cm s⁻¹
812 in the ICW. In the same study, the time-averaged zonal velocity field deduced from
813 trajectories of autonomous floats drifting at 200 m depth (i.e. in the uCW) shows peak
814 eastward flows of 5 cm s⁻¹ again at 14°N. Furthermore, the average zonal flow

815 computed from several meridional sections, carried out during different seasons
816 between 1999 and 2008 and between 28°W and 23°W [Brandt *et al.*, 2010], displays an
817 intense eastward mean flow at 14°N, exceeding 10 cm s⁻¹ in the whole CW stratum.
818 Brandt *et al.* [2010] suggested this current was a recirculation around the Cape Verde
819 Islands but our results show that it flows all the way from the western Atlantic margin to
820 the African continent, although it also includes water recirculating from the south.

821
822 A number of observations [Stramma *et al.*, 2005, 2008b; Brandt *et al.*, 2010; Hahn *et*
823 *al.*, 2014] suggest substantial flow variability between 10°N and 13°N, yet with
824 preferential westward/eastward paths south/north of 12°N, similar to the ECCO2 mean
825 field (Figure 13a). North of the Cape Verde Islands, there are very few velocity
826 observations. A Lowered ADCP (LADCP) section along 28°W in summer 2003
827 displayed a dominant mean eastward flow between 12°N and 18°N only for the 300-600
828 m layer (i.e. roughly the ICW stratum) with velocities at 14°N and 17°N above 5 cm s⁻¹
829 [Stramma *et al.*, 2008b], again in agreement with the ECCO2 results.

830
831 The nNECC is also realistically reproduced in the model, located between 8°N and 9°N
832 and covering most of the thermocline. However, further south, important discrepancies
833 with observations appear. The most notable is the absence of the Equatorial
834 Intermediate Current within the ICW. The NEUC is reproduced somewhat further south
835 than observed, connecting at 2°N with the North Intermediate CounterCurrent, which
836 does not seem to occur in the real ocean [Brandt *et al.*, 2010]. These issues are likely
837 due to the limited horizontal resolution of ECCO2, as high resolution appears necessary
838 to properly model the intermediate depth equatorial circulation [Duteil *et al.*, 2014].
839 Nevertheless, the Lagrangian pathways (Figure 6) have revealed that the ICW of the
840 naOMZ is only weakly linked to this equatorial region so we expect that the
841 significance of these differences is likely small. This disconnection is evident in the
842 mean meridional velocity field, further supported by the southward extension of NACW
843 along 25°W (Figure 13b).

844
845 The existence of prevailing eastward geostrophic undercurrents far from the equator
846 (north of 10°N), as calculated using the Argo program *T/S* profiles, has been recently
847 reported for the North Pacific Ocean by Qiu *et al.* [2013a, 2013b]. These authors found
848 subsurface eastward jets located at 9°N, 13°N and 18°N in the western Pacific margin.

849 The vertical extension of these jets may reach down to 1000 m, with the upper limit
850 typically varying between $\sigma_{26.0}$ and $\sigma_{27.0}$ and shoaling eastwards. These "NEUC
851 jets", as *Qiu et al.*, [2013a, 2013b] dubbed them, seem to be good candidates for the
852 eastward currents observed north of 10°N in the Atlantic ECCO2 field, though with
853 several significant differences. They almost surface south of the Cape Verde Islands,
854 likely due to the location of the Trade Wind Convergence Zone in the eastern Atlantic,
855 further north than in the eastern Pacific; the several current cores at nearby latitudes in
856 the eastern Atlantic (25°W) may actually be related to the presence of the Cape Verde
857 Islands.

858
859 A major current is centred at 14°N, appearing as the most intense eastward flow within
860 the CW stratum north of 5°N (Figure 13a). A southern branch is also discerned at 12°N,
861 mostly within the uCW. Other branches are detected north of the Cape Verde Islands
862 flowing below $\sigma_{26.8}$ and centred at 18°N, and between the islands at 16°N. Since the
863 Atlantic NEUC traditionally refers to the undercurrent at 4°N [*Stramma and Schott*,
864 1999], we refer to all these northern flows as the Cape Verde Current (CVC) System,
865 with the southern (sCVC), central (CVC) and northern (nCVC) branches as shown in
866 Figure 13.

867

868

869

870 **6. Discussion and conclusions**

871

872 The analysis of a comprehensive *T/S* dataset confirms the existence of a permanent
873 abrupt thermohaline transition at $\sigma_{26.8}$ (about 300 m depth) in the eastern tropical
874 North Atlantic Ocean. The water mass analysis reveals the predominance of SACW in
875 the uCW ($\sigma_{26.8}$ to $\sigma_{26.3}$) and an abrupt increase in the contribution of NACW when
876 entering the ICW ($\sigma_{26.8}$ to $\sigma_{27.15}$). The maximum proportion of NACW (50%) is
877 reached at the core of the naOMZ (at $\sigma_{27.1}$), where minimal oxygen content is found.
878 Such a markedly different water mass composition suggests that distinct circulation
879 patterns rule the uCW and ICW, with a potentially important role of previously
880 unreported water transfer from the well-ventilated northern subtropical gyre into the
881 naOMZ core. In order to understand the development of these observational features,

882 we have performed an analysis of the numerical Lagrangian trajectories, computed with
883 ECCO2 velocity field, that end up within the naOMZ.

884

885 The Lagrangian simulations reveal distinct pathways in the upper and lower CW layers
886 (as clearly evidenced in the animation found in the Supplementary Materials). In
887 agreement with previous studies [*Stramma et al.*, 2008b], the water mass supply within
888 the uCW to the naOMZ is mainly (56%) carried by the nNECC and the northward
889 branching of the NEUC, with a predominant contribution of southern origin particles.
890 However, within the ICW these jets largely reduce their contribution in accordance with
891 an enhancement of jets located further north, at the same time that the proportion of
892 northern origin particles increase abruptly. In fact, more than two thirds of the total
893 water supply within this layer occurs north of 10°N, mainly via an eastward flow
894 centred at 14°N (29%) and flows located further north (as much as 18°N) that are fed by
895 waters recirculating from the northern subtropical gyre (30%). The existence of
896 subsurface geostrophic eastward jets, north of 10°N and below the westward flow of the
897 subtropical gyre, have been recently pointed out for the North Pacific Ocean [*Qiu et al.*,
898 2013a]. In the North Atlantic, repeated velocity observations along 23°W have also
899 revealed a predominant eastward flow centred at 14°N [*Brandt et al.*, 2010]. North of
900 the Cape Verde Islands, velocity observations are scarce to validate the existence of
901 these jets. Nevertheless, we show that the high contribution of northern origin particles
902 within these northern eastward flows, here referred as the Cape Verde Current System,
903 accurately accounts for the increased proportion of NACW observed to occur in the
904 ICW. Such a substantial northern supply within the ICW stratum presents a new
905 perspective on the patterns of naOMZ ventilation.

906

907 In contrast with previous Eulerian studies, the Lagrangian description simultaneously
908 incorporates the mean flow seasonal variability, the diapycnal fluxes and the mesoscale
909 eddy-field. Thus, a comparison of different Lagrangian simulations of increased
910 complexity allows isolation of the contribution of the isopycnal/diapycnal fluxes and
911 the model subgrid-scale horizontal eddy diffusion in the water supply to the naOMZ, as
912 briefly discussed next.

913

914 The distinct isopycnal circulation patterns of the uCW and ICW lead to the abrupt
915 thermohaline transition at $\sigma_{26.8}$, smoothed out by diapycnal fluxes through the

916 interlayer exchange of particles. The diapycnal fluxes included in our Lagrangian
917 experiments are based on meso- and regional-scale diapycnal motions that appear to
918 play a remarkable role in the renewal of the naOMZ thermocline. The regional
919 diapycnal velocities have opposite prevailing signs within the two CW layers, affecting
920 the water renewal rate of the naOMZ. In particular, for the sluggish ICW there is
921 predominant downwelling along the trajectories, from shallower and faster to deeper
922 and slower density levels, leading to a water supply enhancement of 20% solely due to
923 diapycnal fluxes. This result points to the significant role that diapycnal fluxes play in
924 the water renewal of the naOMZ.

925

926 *Hahn et al.* [2014] have shown, through the analysis of the meridional variability in the
927 oxygen field, the relevance of meridional eddy stirring. In our case, the non-fully eddy
928 resolving ECCO2 field is unable to correctly reproduce the water mass composition of
929 the naOMZ. Nevertheless, the addition of subgrid-scale diffusion leads to the accurate
930 simulation of the observational hydrographic profiles. A major consequence of this
931 added diffusion is the reduction of the water renewal times (by 25%) due to an
932 enhanced water transfer from the meridional boundaries of the naOMZ, i.e. the
933 NEUC/nNECC region at the south and the subtropical gyre at the north.

934

935 The water mass pathways to the naOMZ, together with the main elements in its
936 thermocline renewal, are sketched within the general circulation of the eastern tropical
937 North Atlantic Ocean in Figure 14. The circulation in the uCW appears embedded
938 within a broad cyclonic pattern, with the eastward NEUC and nNECC flows as the
939 southern limb and the westward NEC as the northern arm. Previous studies have always
940 related this scheme to the local, seasonal and shallow wind-driven Guinea Dome
941 [*Stramma et al.*, 2005, 2008b; *Karstensen et al.* 2008]. However, the relatively deep
942 (reaching 300 m) vertical extent and much broader cyclonic circulation in the uCW,
943 together with the horizontal distribution of the ECCO2 vertical velocities, suggest that
944 the water supply in this layer is driven by the large-scale subtropical cell [*Zhang et al.*,
945 2003; *Schott et al.*, 2004].

946

947 The ICW circulation pattern is markedly different from that of the uCW. The ICW (1) is
948 characterized by much longer residence time (three to four times); (2) includes
949 predominant eastward flows around the Cape Verde Islands and westward currents

further south, sketching a broad anticyclonic circulation; and (3) presents an approximately antisymmetric horizontal distribution in the vertical velocities and layer thicknesses of both layers. These features have led us to hypothesize the existence of a lower subtropical cell within the ICW, with an inverse but weaker circulation scheme compared to the uCW and analogous to the equatorial stacked tropical cells proposed by Wang [2005]. We suggest that both CW strata may interact through a normal baroclinic mode of circulation that leads to opposite circulation patterns

Our results imply that the traditional constraint on OMZ ventilation from the subtropical gyre [Luyten *et al.*, 1983] is limited, at least in the North Atlantic, to those layers above $\sigma_{26.8}$, i.e. in the uCW stratum. In contrast, a weak but significant southward pathway from the subtropical North Atlantic to the naOMZ exists in the ICW. The existence of the proposed inverted cells emerges as a suggestive approach for the study of world OMZs. The substantial interannual and decadal variability of these cells [Schott *et al.*, 2008] likely is a major cause for the changes in oxygen anomalies in the world OMZs during the last decades [Deutsch *et al.*, 2014, Ridder and England, 2014].

Acknowledgements

This research has been funded by the Spanish Ministerio de Economía y Competitividad through projects MOC2 (CTM2008-06438-C02-01) and TIC-MOC (CTM2011- 28867). J. Peña-Izquierdo has been supported through a FPI pre-doctoral grant linked to MOC2. E. van Sebille was supported by the Australian Research Council via grant DE130101336. The authors acknowledge the NODC and Argo Program for making hydrographic data freely available (<http://www.nodc.noaa.gov> and <http://www.coriolis.eu.org>). We also thank the ECCO2/NASA program for providing the numerical assimilative simulation via their web page (<http://ecco2.jpl.nasa.gov/products/>). We would also like to sincerely thank our three reviewers for many useful comments and suggestions to an original version of this paper.

983

984

985

986

987

988

989 **References**

990

- 991 Banyte, D., T. Tanhua, M. Visbeck, D. W. R. Wallace, J. Karstensen, G. Krahmann, A.
992 Schneider, L. Stramma, and M. Dengler (2012), Diapycnal diffusivity at the upper
993 boundary of the tropical North Atlantic oxygen minimum zone, *J. Geophys. Res.*
994 *Ocean.*, 117(C9), n/a–n/a, doi:10.1029/2011JC007762.
- 995 Barton, E. (1989), The Poleward undercurrent on the eastern boundary of the
996 subtropical north atlantic, in *Coastal and Estuarine Studies*, edited by C. N. K. M.
997 S.Neshyba, R.L., Smith, pp. 82–95, Springer-Verlag.
- 998 Blanke, B., M. Arhan, G. Madec, and S. Roche (1999), Warm Water Paths in the
999 Equatorial Atlantic as Diagnosed with a General Circulation Model, *J. Phys.*
1000 *Oceanogr.*, 29(11), 2753–2768.
- 1001 Bopp, L., C. Le Que, M. Heimann, A. C. Manning, and P. Monfray (2002), Climate-
1002 induced oceanic oxygen fluxes : Implications for the contemporary carbon budget,
1003 , 16(2).
- 1004 Brandt, P., V. Hormann, A. Körtzinger, M. Visbeck, G. Krahmann, L. Stramma, R.
1005 Lumpkin, and C. Schmid (2010), Changes in the Ventilation of the Oxygen
1006 Minimum Zone of the Tropical North Atlantic, *J. Phys. Oceanogr.*, 40(8), 1784–
1007 1801, doi:10.1175/2010JPO4301.1.
- 1008 Brandt, P. et al. (2014), On the role of circulation and mixing in the ventilation of
1009 oxygen minimum zones with a focus on the eastern tropical North Atlantic,
1010 *Biogeosciences Discuss.*, 11(8), 12069–12136, doi:10.5194/bgd-11-12069-2014.
- 1011 Deutsch, C., H. Brix, T. Ito, H. Frenzel, and L. Thompson (2011), Climate-forced
1012 variability of ocean hypoxia., *Science*, 333(6040), 336–9,
1013 doi:10.1126/science.1202422.
- 1014 Döös, K., J. Nycander, and a. C. Coward (2008), Lagrangian decomposition of the
1015 Deacon Cell, *J. Geophys. Res.*, 113(C7), C07028, doi:10.1029/2007JC004351.
- 1016 Döös, K., V. Rupolo, and L. Brodeau (2011), Dispersion of surface drifters and model-
1017 simulated trajectories, *Ocean Model.*, 39(3-4), 301–310,
1018 doi:10.1016/j.ocemod.2011.05.005.
- 1019 Duteil, O., F. U. Schwarzkopf, C. W. Böning, and A. Oschlies (2014), Major role of the
1020 equatorial current system in setting oxygen levels in the eastern tropical Atlantic
1021 Ocean: A high-resolution model study, *Geophys. Res. Lett.*, 41(6), 2033–2040,
1022 doi:10.1002/2013GL058888.
- 1023 El moussaoui, a., M. Arhan, and a. M. Treguier (2005), Model-inferred upper ocean
1024 circulation in the eastern tropics of the North Atlantic, *Deep Sea Res. Part I*
1025 *Oceanogr. Res. Pap.*, 52(7), 1093–1120, doi:10.1016/j.dsr.2005.01.010.

- 1026 Fischer, T., D. Banyte, P. Brandt, M. Dengler, G. Krahmann, T. Tanhua, and M.
1027 Visbeck (2013), Diapycnal oxygen supply to the tropical North Atlantic oxygen
1028 minimum zone, *Biogeosciences*, 10(7), 5079–5093, doi:10.5194/bg-10-5079-2013.
- 1029 Fraga F. (1974), Distribution des masses d'eau dans l'upwelling de mauritanie,
1030 *Tethysethys*, 6, 5–10.
- 1031 Fratantoni, D. M., W. E. Johns, T. L. Townsend, and H. E. Hurlburt (2000), Low-
1032 Latitude Circulation and Mass Transport Pathways in a Model of the Tropical
1033 Atlantic Ocean, *J. Phys. Oceanogr.*, 30, 1944–1966.
- 1034 Fu, L.-L. (2009), Pattern and velocity of propagation of the global ocean eddy
1035 variability, *J. Geophys. Res.*, 114(C11), C11017, doi:10.1029/2009JC005349.
- 1036 Garcia, H., A. Cruzado, L. Gordon, and J. Escanez (1998), Decadal-scale chemical
1037 variability in the subtropical North Atlantic deduced from nutrient and oxygen
1038 data, *J. Geophys. Res.*, 103(C2), 2817, doi:10.1029/97JC03037.
- 1039 Gnanadesikan, A., J. L. Russell, F. Zeng, and G. Fluid (2007), How does ocean
1040 ventilation change under global warming, *Ocean Sci.* 3, 43–53.
- 1041 Gouretski, V. and Koltermann, P. (2004), *WOCE Global Hydrographic Climatology—A*
1042 *Technical Report. Berichte des Bundesamtes für Seeschifffahrt und Hydrographie.*
- 1043 Griffies, S. M., R. C. Pacanowski, and R. W. Hallberg (2000), Spurious Diapycnal
1044 Mixing Associated with Advection in a z -Coordinate Ocean Model, *Mon. Weather*
1045 *Rev.*, 128, 538–564.
- 1046 Hahn, J., P. Brandt, R. J. Greatbatch, G. Krahmann, and a. Körtzinger (2014), Oxygen
1047 variance and meridional oxygen supply in the Tropical North East Atlantic oxygen
1048 minimum zone, *Clim. Dyn.*, doi:10.1007/s00382-014-2065-0.
- 1049 Hazeleger, W., and S. Drijfhout (2006), Subtropical cells and meridional overturning
1050 circulation pathways in the tropical Atlantic, *J. Geophys. Res.*, 111(C3), C03013,
1051 doi:10.1029/2005JC002942.
- 1052 Joos, F., G.-K. Plattner, T. F. Stocker, A. Körtzinger, and D. W. R. Wallace (2003),
1053 Trends in marine dissolved oxygen: Implications for ocean circulation changes and
1054 the carbon budget, *Eos, Trans. Am. Geophys. Union*, 84(21), 197,
1055 doi:10.1029/2003EO210001.
- 1056 Karstensen, J., L. Stramma, and M. Visbeck (2008), Oxygen minimum zones in the
1057 eastern tropical Atlantic and Pacific oceans, *Prog. Oceanogr.*, 77(4), 331–350,
1058 doi:10.1016/j.pocean.2007.05.009.
- 1059 Kirchner, K., M. Rhein, S. Hüttl-Kabus, and C. W. Böning (2009), On the spreading of
1060 South Atlantic Water into the Northern Hemisphere, *J. Geophys. Res.*, 114(C5),
1061 C05019, doi:10.1029/2008JC005165.

- 1062 Lam, P., and M. M. M. Kuypers (2011), Microbial Nitrogen Cycling Processes in
1063 Oxygen Minimum Zones, *Ann. Rev. Mar. Sci.*, 3(1), 317–345,
1064 doi:10.1146/annurev-marine-120709-142814.
- 1065 Lázaro, C., M. J. Fernandes, a. M. P. Santos, and P. Oliveira (2005), Seasonal and
1066 interannual variability of surface circulation in the Cape Verde region from 8 years
1067 of merged T/P and ERS-2 altimeter data, *Remote Sens. Environ.*, 98(1), 45–62,
1068 doi:10.1016/j.rse.2005.06.005.
- 1069 Lu, P., J. P. McCreary, and B. A. Klinger (1998), Meridional Circulation Cells and the
1070 Source Waters of the Pacific Equatorial Undercurrent, *J. Phys. Oceanogr.*, 28, 62–
1071 84.
- 1072 Luyten, J. R., J. Pedlosky, and H. Stommel (1983), The Ventilated Thermocline, *J Phys.*
1073 *Ocean.*, 13, 292–309, doi:http://dx.doi.org/10.1175/1520-
1074 0485(1983)013<0292:TVT>2.0.CO;2.
- 1075 Mackas, D. L., K. L. Denman, and A. F. Bennett (1987), Least squares multiple tracer
1076 analysis of water mass composition, *J. Geophys. Res.*, 92(C3), 2907,
1077 doi:10.1029/JC092iC03p02907.
- 1078 Millero, F.J., R. Feistel, D. G. Wright, T. J. McDougall (2008), The composition of
1079 Standard Seawater and the definition of the Reference-Composition Salinity Scale,
1080 *Deep Sea Res. Part I Oceanogr. Res. Pap.*, 55(1), 50-72.
- 1081 Marshall, J., A. Adcroft, C. Hill, L. Perelman, and C. Heisey (1997), A finite-volume,
1082 incompressible Navier Stokes model for studies of the ocean on parallel
1083 computers, *J. Geophys. Res.*, 102(C3), 5753, doi:10.1029/96JC02775.
- 1084 Matear, R. J., and a. C. Hirst (2003), Long-term changes in dissolved oxygen
1085 concentrations in the ocean caused by protracted global warming, *Global*
1086 *Biogeochem. Cycles*, 17(4), n/a–n/a, doi:10.1029/2002GB001997.
- 1087 Mittelstaedt, E. (1991), The ocean boundary along the northwest African coast:
1088 Circulation and oceanographic properties at the sea surface, *Prog. Oceanogr.*,
1089 26(4), 307–355.
- 1090 Oeschies, A., K. G. Schulz, U. Riebesell, and A. Schmittner (2008), Simulated 21st
1091 century's increase in oceanic suboxia by CO₂-enhanced biotic carbon export,
1092 *Global Biogeochem. Cycles*, 22(4), GB4008, doi:10.1029/2007GB003147.
- 1093 Paris, C. B., J. Helgers, E. van Sebille, and A. Srinivasan (2013), Connectivity
1094 Modeling System: A probabilistic modeling tool for the multi-scale tracking of
1095 biotic and abiotic variability in the ocean, *Environ. Model. Softw.*, 42, 47–54,
1096 doi:10.1016/j.envsoft.2012.12.006.
- 1097 Pastor, M. V., J. Peña-Izquierdo, J. L. Pelegrí, and Á. Marrero-Díaz (2012), Meridional
1098 changes in water mass distributions off NW Africa during November 2007/2008,
1099 *Ciencias Mar.*, 38, 223–244.

- 1100 Paulmier, a., D. Ruiz-Pino, and V. Garçon (2011), CO₂ maximum in the oxygen
1101 minimum zone (OMZ), *Biogeosciences*, 8(2), 239–252, doi:10.5194/bg-8-239-
1102 2011.
- 1103 Peña-Izquierdo, J., J. L. Pelegrí, M. V. Pastor, P. Castellanos, M. Emelianov, M.
1104 Gasser, J. Salvador, and E. Vázquez-Domínguez (2012), The continental slope
1105 current system between Cape Verde and the Canary Islands, *Sci. Mar.*, 76(S1), 65–
1106 78, doi:10.3989/scimar.03607.18C.
- 1107 Poole, R., and M. Tomczak (1999), Optimum multiparameter analysis of the water mass
1108 structure in the Atlantic Ocean thermocline, *Deep Sea Res. Part I Oceanogr. Res.*
1109 *Pap.*, 46(11), 1895–1921, doi:10.1016/S0967-0637(99)00025-4.
- 1110 Qiu, B., D. L. Rudnick, S. Chen, and Y. Kashino (2013a), Quasi-stationary North
1111 Equatorial Undercurrent jets across the tropical North Pacific Ocean, *Geophys.*
1112 *Res. Lett.*, 40(10), 2183–2187, doi:10.1002/grl.50394.
- 1113 Qiu, B., S. Chen, and H. Sasaki (2013b), Generation of the North Equatorial
1114 Undercurrent Jets by Triad Baroclinic Rossby Wave Interactions, *J. Phys.*
1115 *Oceanogr.*, 43(12), 2682–2698, doi:10.1175/JPO-D-13-099.1.
- 1116 Reid, J. L. (1994), On the total geostrophic circulation of the North Atlantic Ocean:
1117 Flow patterns, tracers, and transports, *Prog. Oceanogr.*, 33(1), 1–92,
1118 doi:10.1016/0079-6611(94)90014-0.
- 1119 Rhein, M., K. Kirchner, C. Mertens, R. Steinfeldt, M. Walter, and U. Fleischmann-
1120 Wischnath (2005), Transport of South Atlantic water through the passages south of
1121 Guadeloupe and across 16°N, 2000–2004, *Deep Sea Res. Part I Oceanogr. Res.*
1122 *Pap.*, 52(12), 2234–2249, doi:10.1016/j.dsr.2005.08.003.
- 1123 Ridder, N. N., and M. H. England (2014), Sensitivity of ocean oxygenation to variations
1124 in tropical zonal wind stress magnitude, *Global Biogeochem. Cycles*, 28,
1125 doi:10.1002/2013GB004708.
- 1126 Schott, F. A., J. P. McCreary, and G. C. Johnson (2004), Shallow Overturning
1127 Circulations of the Tropical- Subtropical Oceans tropical subduction regions of
1128 both hemispheres to the eastern , equatorial upwelling,
- 1129 Schott, F. a., L. Stramma, W. Wang, B. S. Giese, and R. Zantopp (2008), Pacific
1130 Subtropical Cell variability in the SODA 2.0.2/3 assimilation, *Geophys. Res. Lett.*,
1131 35(10), L10607, doi:10.1029/2008GL033757.
- 1132 Siedler, G., N. Zangenberg, and R. Onken (1992), Seasonal Changes in the Tropical
1133 Atlantic Circulation: Observation and Simulation of the Guinea Dome, *J. Geophys.*
1134 *Res. Ocean.*, 97, 703–715.
- 1135 Stramma, L., and F. Schott (1999), The mean flow field of the tropical Atlantic Ocean,
1136 *Deep Sea Res. Part II Top. Stud. Oceanogr.*, 46(1-2), 279–303,
1137 doi:10.1016/S0967-0645(98)00109-X.

- 1138 Stramma, L., S. Hüttl, and J. Schafstall (2005), Water masses and currents in the upper
1139 tropical northeast Atlantic off northwest Africa, *J. Geophys. Res.*, *110*(C12),
1140 C12006, doi:10.1029/2005JC002939.
- 1141 Stramma, L., G. C. Johnson, J. Sprintall, and V. Mohrholz (2008a), Expanding oxygen-
1142 minimum zones in the tropical oceans., *Science*, *320*(5876), 655–8,
1143 doi:10.1126/science.1153847.
- 1144 Stramma, L., P. Brandt, J. Schafstall, F. Schott, J. Fischer, and A. Körtzinger (2008b),
1145 Oxygen minimum zone in the North Atlantic south and east of the Cape Verde
1146 Islands, *J. Geophys. Res.*, *113*(C4), C04014, doi:10.1029/2007JC004369.
- 1147 Stramma, L., M. Visbeck, P. Brandt, T. Tanhua, and D. Wallace (2009), Deoxygenation
1148 in the oxygen minimum zone of the eastern tropical North Atlantic, *Geophys. Res.*
1149 *Lett.*, *36*(20), L20607, doi:10.1029/2009GL039593.
- 1150 Tomczak, M. (1981), An analysis of mixing in the frontal zone o f South and North
1151 Atlantic Central Water off North - West Africa, *Prog. Oceanogr.*, *10*, 173–192.
- 1152 Tomczak, M., and D. G. B. Large (1989), Multiparameter Analysis of Mixing in the
1153 Thermocline represent of the Eastern Indian Ocean, , *94*(C11), 16,141–16,149.
- 1154 Van Sebille, E., W. E. Johns, and L. M. Beal (2012), Does the vorticity flux from
1155 Agulhas rings control the zonal pathway of NADW across the South Atlantic?, *J.*
1156 *Geophys. Res.*, *117*(C5), C05037, doi:10.1029/2011JC007684.
- 1157 Van Sebille, E., P. Spence, M. R. Mazloff, M. H. England, S. R. Rintoul, and O. a.
1158 Saenko (2013), Abyssal connections of Antarctic Bottom Water in a Southern
1159 Ocean State Estimate, *Geophys. Res. Lett.*, *40*(10), 2177–2182,
1160 doi:10.1002/grl.50483.
- 1161 Vaquer-Sunyer, R., and C. Duarte (2008), Thresholds of hypoxia for marine
1162 biodiversity, *Proc. Natl. Acad. Sci. U. S. A.*, *105*(40), 15452–15457.
- 1163 Voituriez, B., and R. Chuchla (1978), Influence of the Southern Atlantic Central Water
1164 on the distribution of salinity and oxygen in the northeast tropical Atlantic Ocean,
1165 *Deep. Res.*, *25*.
- 1166 Wang, C. (2005), Subthermocline tropical cells and equatorial subsurface
1167 countercurrents, *Deep Sea Res. Part I Oceanogr. Res. Pap.*, *52*(1), 123–135,
1168 doi:10.1016/j.dsr.2004.08.009.
- 1169 Xuang, R. X. (2010), *Ocean Circulation, Wind-Driven and Thermohaline Processes*,
1170 Cambridge University Press, New York.
- 1171 Zhang, D., M. J. McPhaden, and W. E. Johns (2003), Observational Evidence for Flow
1172 between the Subtropical and Tropical Atlantic : The Atlantic Subtropical Cells *, *J.*
1173 *Phys. Oceanogr.*, *33*, 1783–1797.
- 1174

1176

1177 **List of tables**

1178 Table 1. Contribution (%) of the different flows to the water mass supply (WM) of
1179 upper Central Water (uCW) and lower Central Water (lCW) to the naOMZ across
1180 the control section* (see subsection 4.4).

1181

1182 **List of Figures**

1183 Figure 1. Schematic circulation pattern in the tropical Atlantic Ocean as derived from
1184 previous studies, overlying the climatological oxygen content of the 200 to 500 m
1185 layer. The naOMZ box (Lagrangian particles release region) is indicated by a white
1186 box. The frontal zone between SACW and NACW is shown as a white dashed
1187 line; C.V.I. refers to the Cape Verde Islands. Main currents: North Brazil Current
1188 (NBC), Equatorial Undercurrent (EUC), North Equatorial Undercurrent (NEUC),
1189 North Intermediate Countercurrent (NICC), northern branch of the North
1190 Equatorial Countercurrent (nNECC), Mauritanian Current (MC), Poleward
1191 Undercurrent (PUC), Guinea Dome (GD) and North Equatorial Current (NEC).

1192 Figure 2. T/S diagrams for all available profiles inside each 10° latitude \times 7° longitude
1193 bin. Each box shows the definition of SACW/NACW (red/blue lines), the
1194 isopycnal limits of the central water stratum ($\sigma_{26.3}$ to $\sigma_{27.15}$, green lines) and the
1195 number of observational profiles.

1196 Figure 3. Top panels: Location of the T/S profiles with a marked thermohaline
1197 transition, defined as a change in the slope of the T/S profiles greater than 0.1°C
1198 per salinity unit with respect to the NACW and SACW pre-defined slopes. The
1199 colored colors indicate the density level where the transition is found. Middle
1200 panels: T/S diagrams of those profiles located in the A, B and C regions shown in
1201 the top-left panel, plotted according to the black-grey code shown inside each box;
1202 regions B and C include 135 and 109 profiles, respectively. Bottom panel: Mean
1203 profiles of NACW proportion and oxygen content for regions B and C; the dashed
1204 lines denote one standard deviation. The left panels are for the observational data

1205 set, while the right panels are for the ECCO2 model output. Note that the ECCO2
1206 model does not include the oxygen field.

1207 Figure 4. Distribution of CWs in the tropical Atlantic Ocean. Left panels: Proportion of
1208 NACW as deduced from the water mass analysis at (top panel) $\sigma_{26.5}$ and (bottom
1209 panel) $\sigma_{27.1}$, where the oxygen content in the uCW and lCW layers is minimum.
1210 Black contours show the climatological oxygen field at the respective density
1211 levels. Right panels: Standard deviation of the NACW proportion within bins of
1212 2.5° latitude \times 5° longitude; all bins include more than 50 observations. Black
1213 contours show the smoothed distribution of NACW after a gridding scheme
1214 algorithm. The SACW proportion always equals the complementary part of the
1215 NACW contribution, i.e. SACW + NACW = 1.

1216 Figure 5. Comparison between the mean observed vertical profile of NACW within the
1217 naOMZ box (black line, with the dashed line showing one standard deviation from
1218 the mean), and the fraction of particles of northern origin entering the naOMZ (the
1219 red/blue lines correspond to particles arriving from north of $20^\circ\text{N}/30^\circ\text{N}$).
1220 Additionally, the green line is calculated as the contribution of NACW particles
1221 that cross into the naOMZ box, and the grey line denotes the fraction of particles
1222 that do not leave the domain during the whole 100 year simulation.

1223 Figure 6. Lagrangian pathways to the naOMZ for the three experiments within the uCW
1224 (top panel) and the lCW (bottom panel). Simulations are from the ISO-K0 (left
1225 panels), the 3D-K0 (middle panels) and the 3D-K100 (right panels) runs. The LSF
1226 is normalized by the total number of particles per layer, i.e. increments between
1227 contours refer to the proportion of particles that flow in between, with LSF values
1228 increasing to the right of the flow. The zero reference LSF is selected in the south-
1229 western corner of the domain, so positive (negative) values of the LSF are related
1230 to southern (northern) origin pathways. The control section used in Figure 8 is
1231 displayed as a black dashed line.

1232 Figure 7. Fraction of the total number of particles (in color) that are found within each
1233 $0.5^\circ \times 0.5^\circ$ horizontal bin, at any time during the whole duration of each simulation,
1234 for the uCW (top panel) and the lCW (bottom panel) strata. Simulations are from
1235 the ISO-K0 (left panels), the 3D-K0 (middle panels) and the 3D-K100 (right

panels) runs. The advection times to the naOMZ box (white-edged box) are displayed with blue contours. For each bin, the advection time is estimated as the median value of the travelling-time distribution that takes particles at the bin location to reach their seeding location.

Figure 8. Water supply across the naOMZ control section in the 3D-K100 simulation. (a) Fraction of the total number of particles crossing the control section at each density level (colored) together with the proportion of observed NACW (blue contours). (b) The normalized local inflow (solid lines) and along-section cumulative inflow (dashed lines) of particles according to level and layer (see inset legend). (c) As in (b) but for particles originated north of 20°N. (d) Average advection times (in years) between the time particles cross the naOMZ control section and the time they reach their seeding location; for comparison, the contour of 0.005 units in the fraction of ingoing particles (displayed in a) is shown with a black line. The control section is displayed in Figure 6.

Figure 9. (a) Potential density distribution for five sets of particles (each set corresponds to a different color) corresponding to 1 and 10 years (dashed and solid lines, respectively) before they reached the naOMZ. Particles within each set end their trajectory in the selected density level ($\sigma_{26.3}$, $\sigma_{26.5}$, $\sigma_{26.7}$, $\sigma_{26.9}$ and $\sigma_{27.1}$). (b) Corresponding cumulative distributions, with circles highlighting the proportion of particles with densities smaller than the final density level. Note that more (less) than 50% of the particles ending at a specific density level above (below) $\sigma_{26.7}$ originally had larger (smaller) densities.

Figure 10. Results from the ISO-K100 and 3D-K100 simulations (blue and red lines, respectively). (a) Temporal increase in the proportion of particles as they fill the naOMZ control region (shown in Figure 6) for three different final density levels; the naOMZ is assumed to be completely renewed when the proportion of particles reaches 100%. (b) Number of years required to fill 30, 50 and 70% of the naOMZ control region, plotted as a function of the final density level. (c) Vertical profile of the contribution of the diapycnal flux to the renewal of the naOMZ (f_{dia}), with positive/negative values representing enhanced/reduced diapycnal water supply; the mean (solid line) and standard deviation (dashed lines) are calculated from the contributions at different times throughout the simulation.

1268 Figure 11. Flow patterns in the northeastern tropical Atlantic Ocean as deduced from
1269 the climatological ECCO2 annual-mean flow field. Vertically-averaged zonal
1270 velocity (in color) for (a) the uCW and (b) the ICW strata; positive values denote
1271 eastward flow. Black contours denote the Eulerian stream function with 0.1 Sv
1272 increments; green contours represent the averaged NACW proportion within the
1273 corresponding layer. (c and d) Analogous plots but for the vertical velocity, with
1274 the positive values denoting upward flow. (e and f) Simplified schemes of the 3D
1275 circulation in both layers.

1276 Figure 12. Annual-mean depth of the (a) $\sigma_{26.8}$ and (b) $\sigma_{27.15}$ density levels,
1277 respectively located at the base of the uCW and ICW layers; the contour intervals
1278 are 4 m and 2 m for the upper and lower layer, respectively. (c and d) Mean
1279 thickness for both the uCW and ICW strata, respectively; contours intervals of 5 m.
1280 (e and f) Planetary component of the potential vorticity for both the uCW and ICW
1281 strata, respectively; green contours represent the average proportion of NACW.

1282 Figure 13. Annual-mean (a) zonal and (b) meridional velocity components along 25°W
1283 as deduced from the ECCO2 model. Positive values denote eastward and
1284 northward flow; contours of 0.02 m s^{-1} are shown with black lines. Thick grey lines
1285 represent the density levels that confine the uCW and ICW layers. The observed
1286 NACW proportion is denoted with green contours. The grey vertical shades
1287 correspond to two of the Cape Verde Islands.

1288 Figure 14. Schematics of the average circulation in the northeastern tropical Atlantic in
1289 the uCW (left) and ICW (right) layers. The distribution of the observed proportion
1290 of NACW is shown with blue-contours. Major pathways to the naOMZ are
1291 highlighted in red. Twisted arrows represent regions where water mass renewal by
1292 eddy diffusion is enhanced.

1293

1294 Table 1. Contribution (%) of the different streams through the control section, supplying
1295 water mass to the naOMZ (WM), for both the upper Central Water (uCW) and
1296 lower Central Water (lCW) strata* (see subsection 4.4).

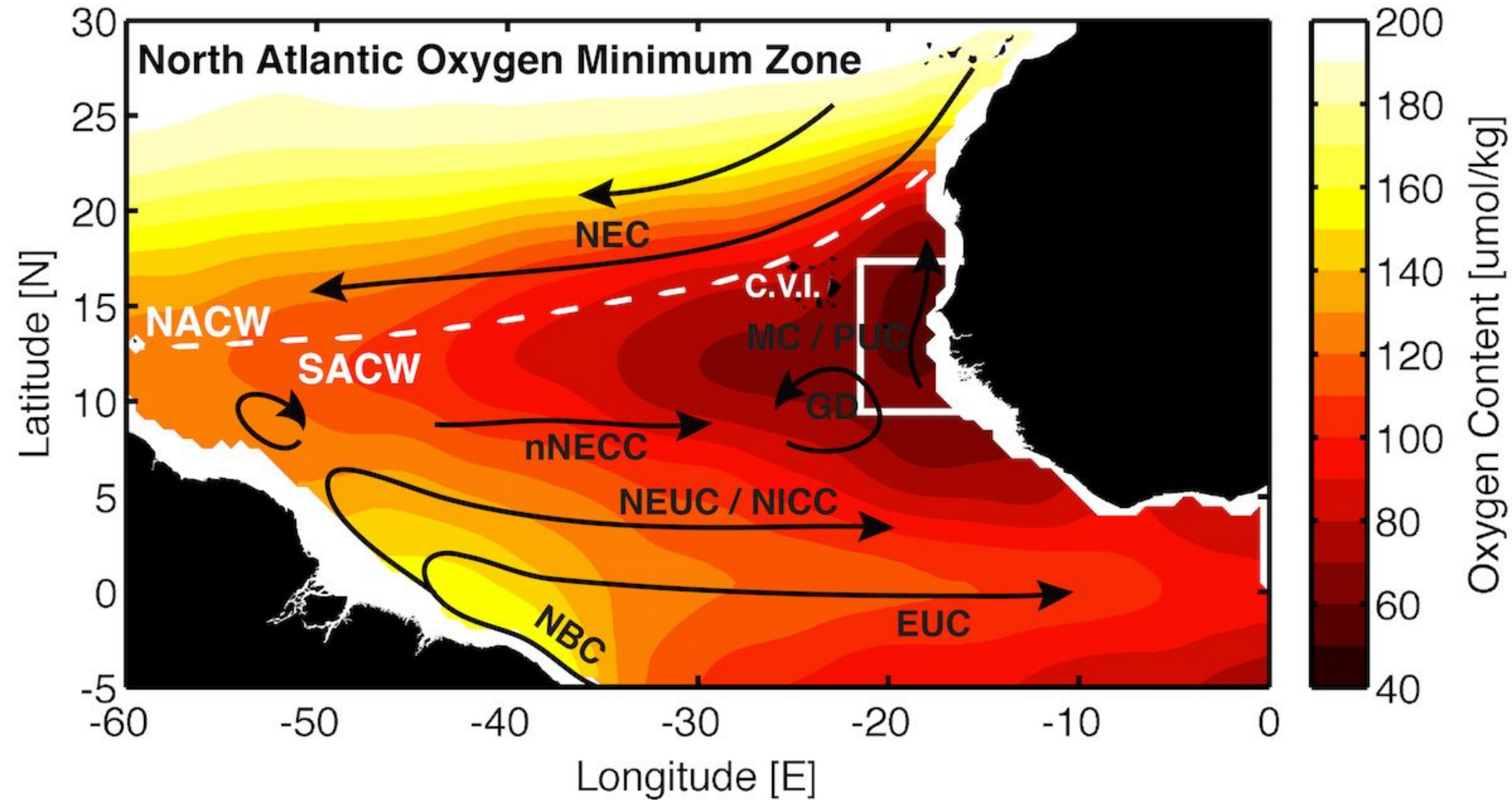
		NEUC/ NICC	nNECC	12°N	14°N	16°N	18°N	20°N
Total	uCW	32 (43)	24 (31)	22 (16)	17 (18)	01 (00)	01 (00)	03 (02)
	lCW	18 (27)	09 (14)	14 (10)	29 (16)	10 (08)	09 (11)	11 (14)
Northern	uCW	00 (00)	00 (00)	01 (01)	03 (02)	00 (00)	00 (00)	03 (02)
	lCW	00 (00)	01 (02)	03 (04)	10 (09)	05 (05)	08 (09)	11 (14)

* The values in parenthesis correspond to the $\sigma_{26.5}$ and $\sigma_{27.1}$ levels and bold numbers emphasize those flows with the highest contributions; northern refers to the proportion of the total flow formed by northern-origin (30°N) particles (Figure 8c).

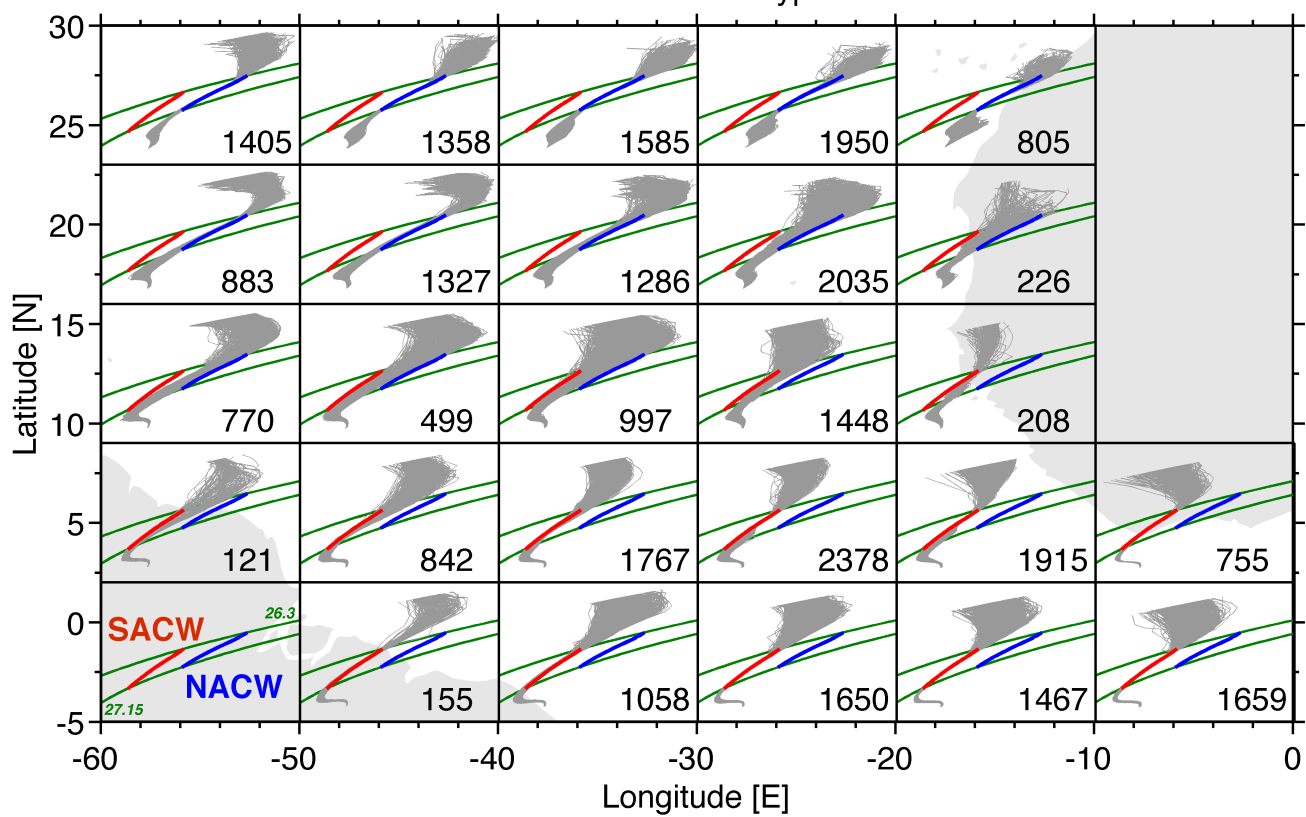
1297

1298

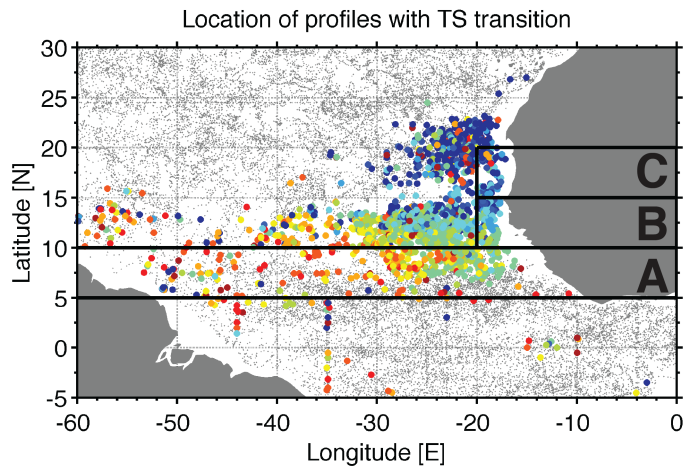
1299



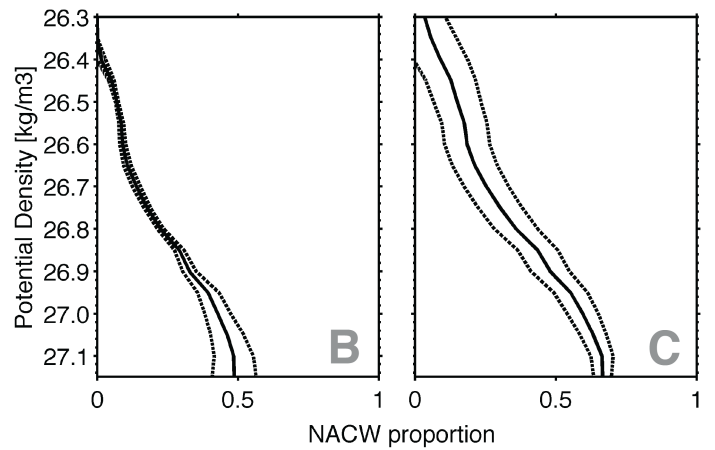
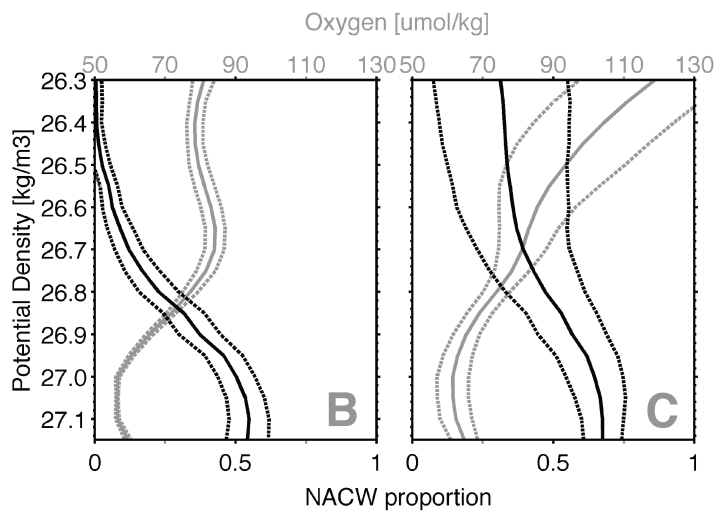
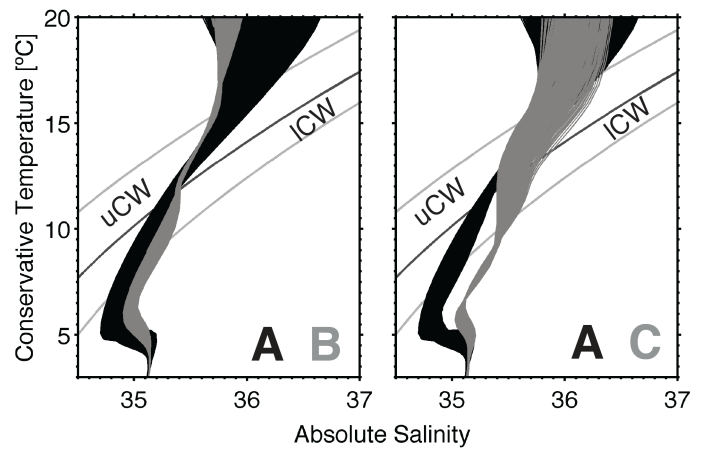
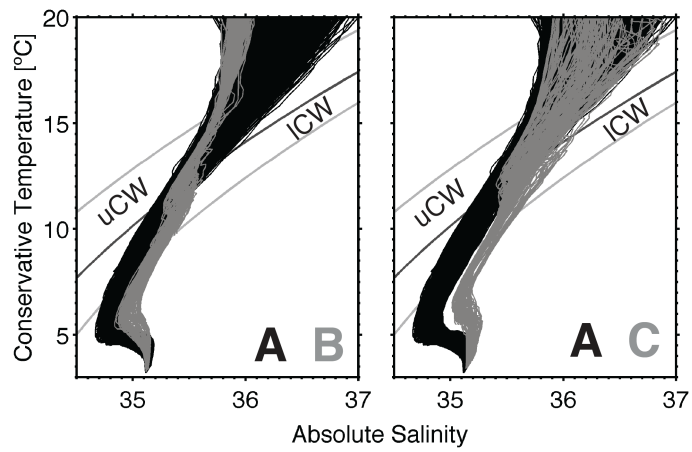
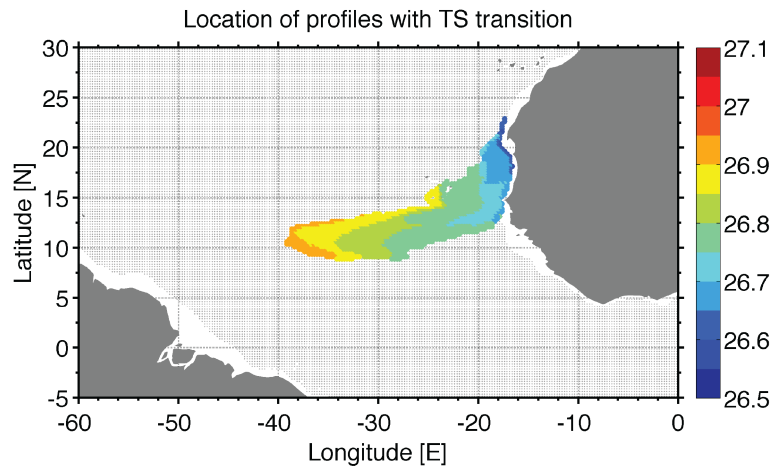
SACW and NACW water types definition



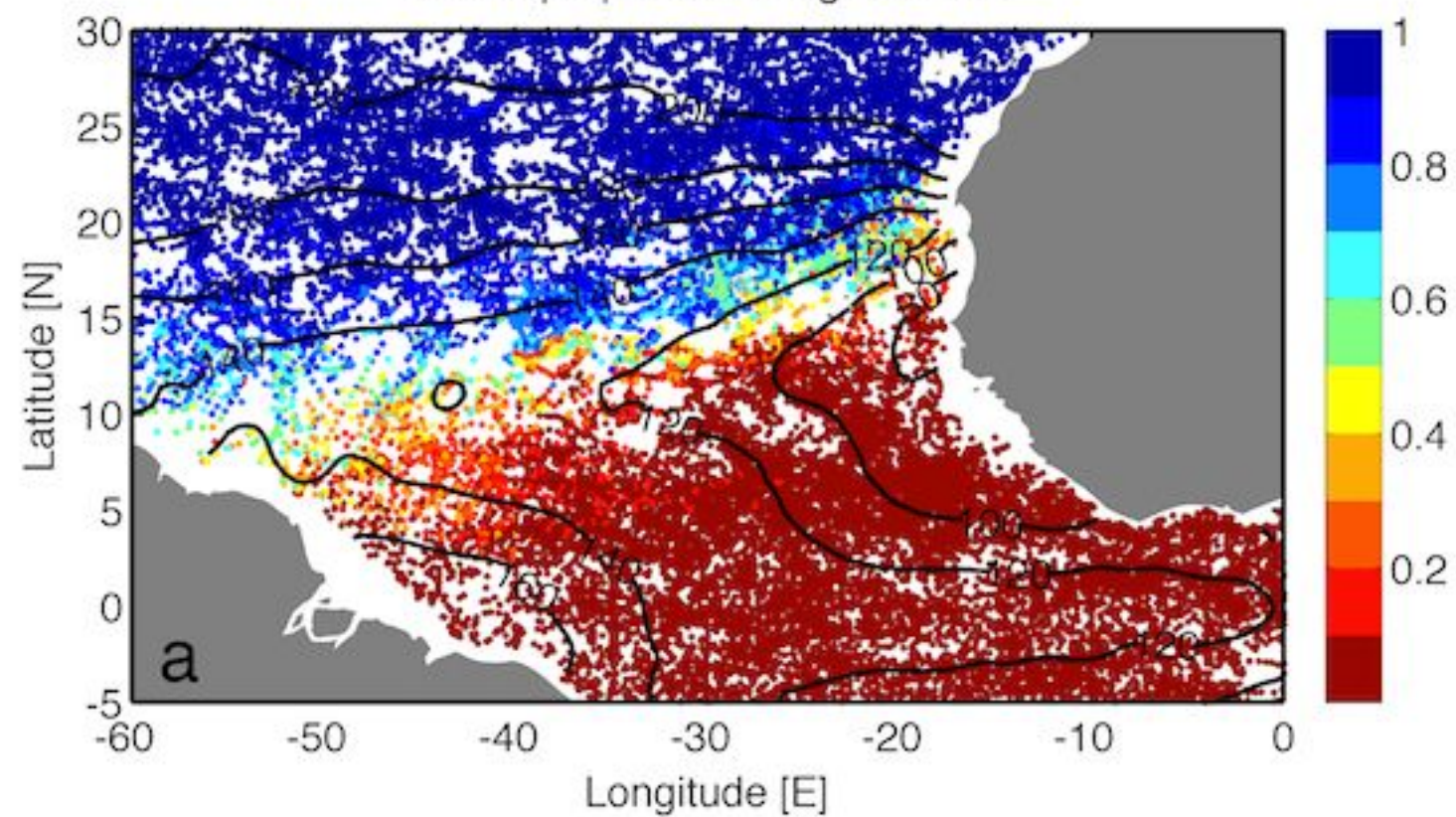
OBSERVATIONS



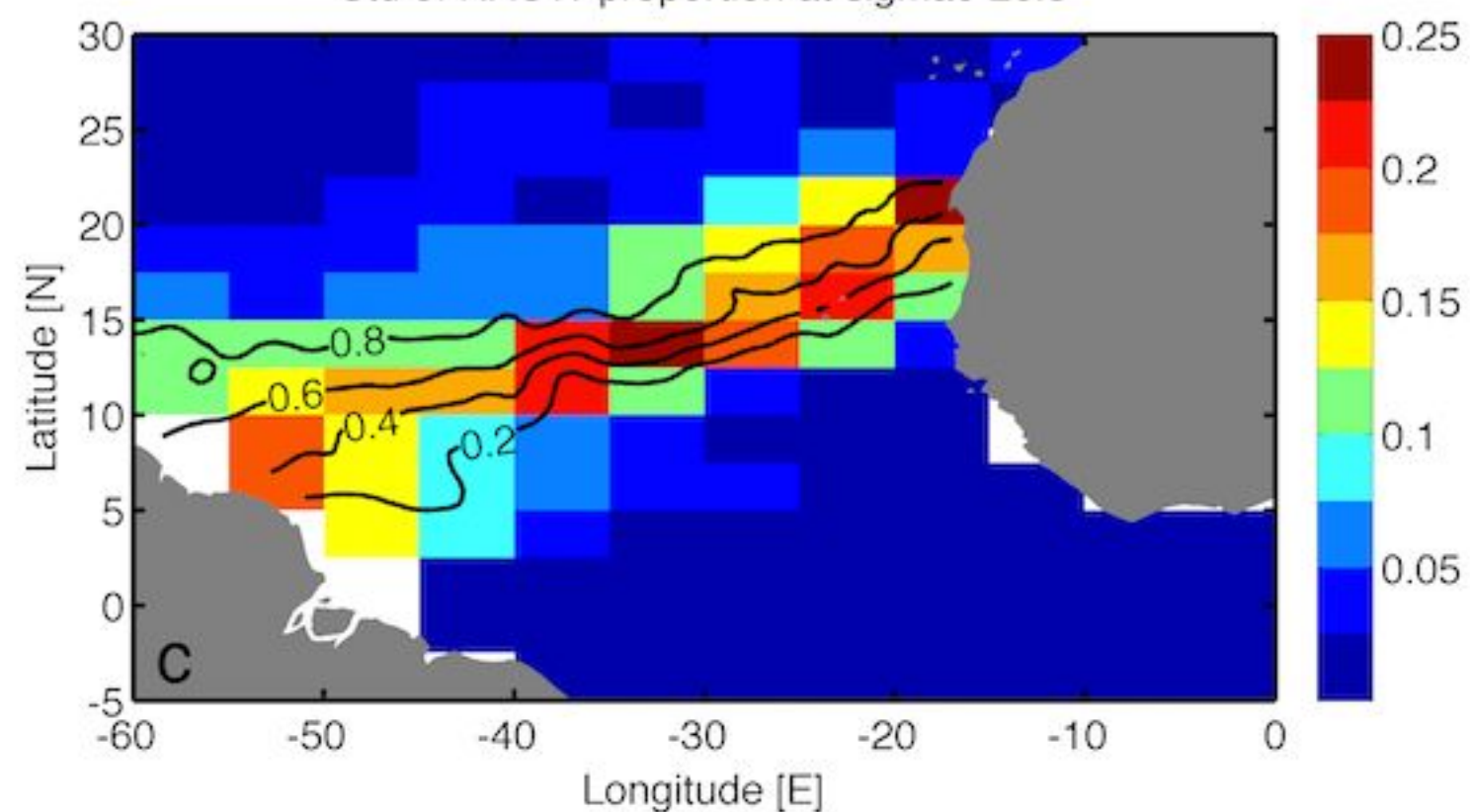
MODEL



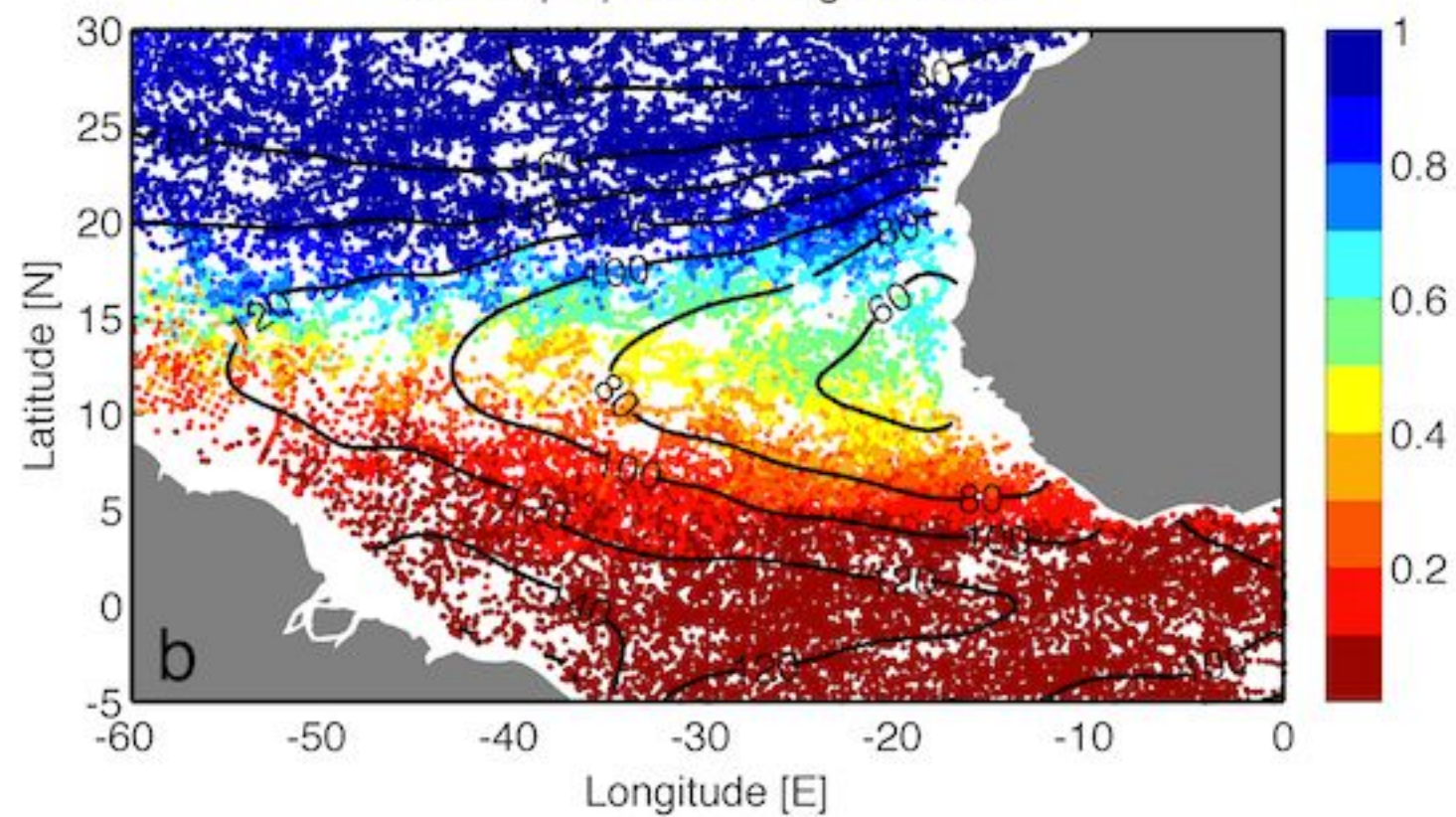
NACW proportion at sigma0 26.5



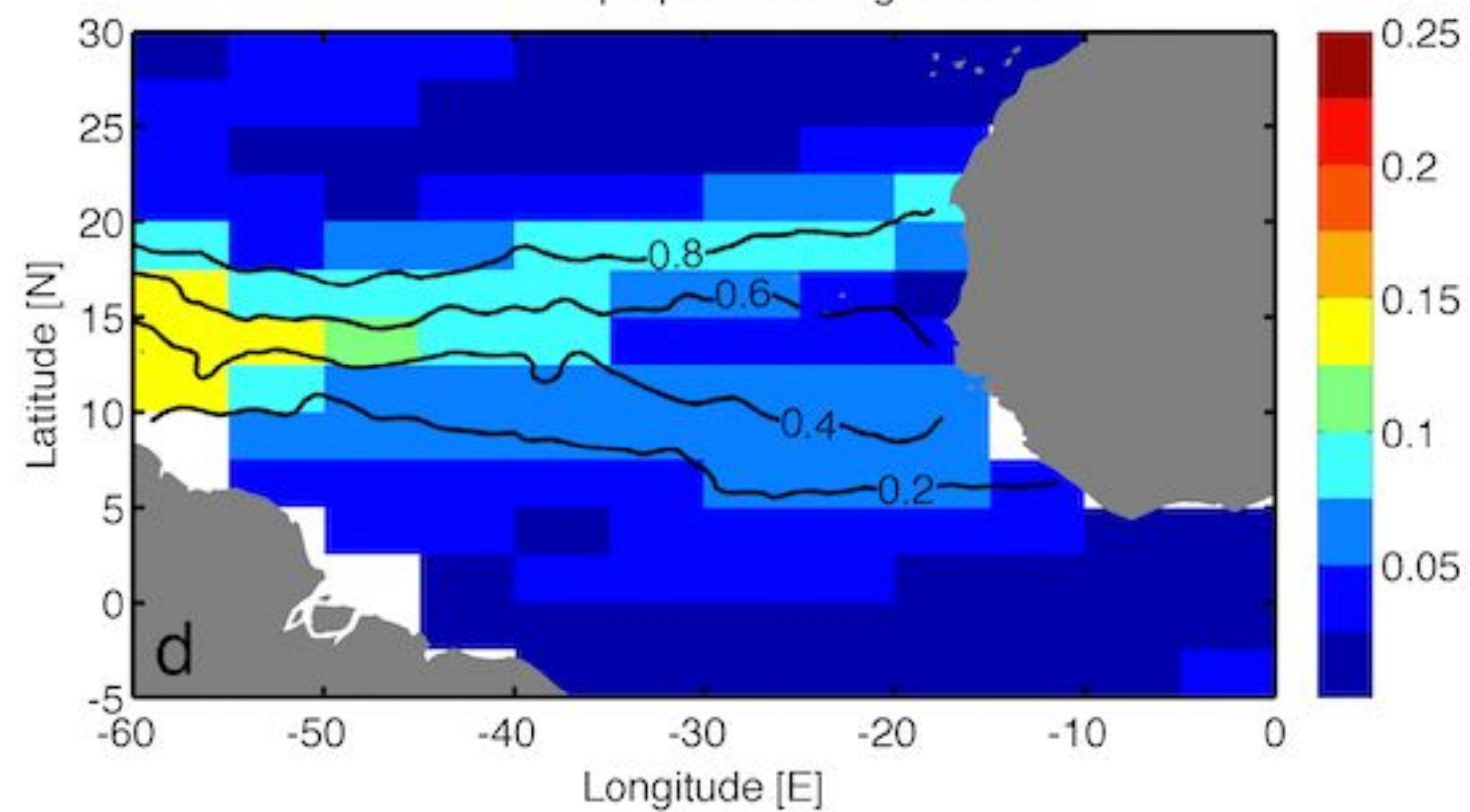
Std of NACW proportion at sigma0 26.5

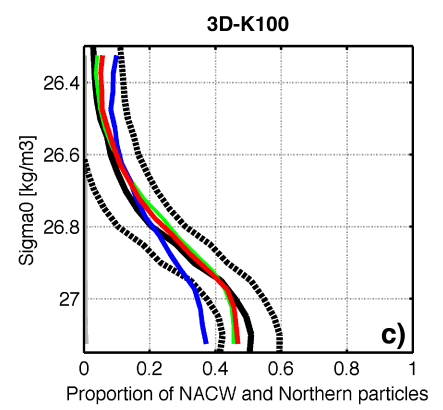
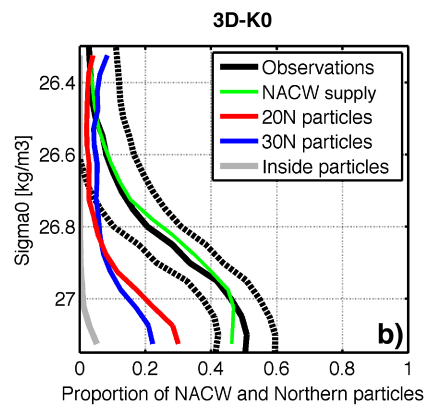
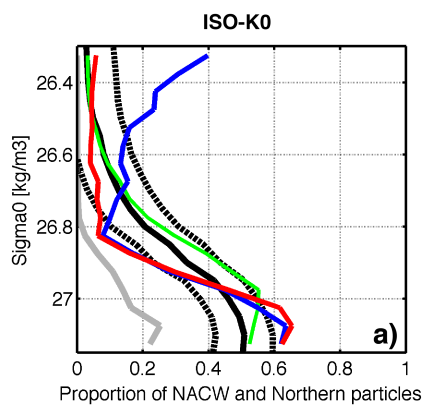


NACW proportion at sigma0 27.1

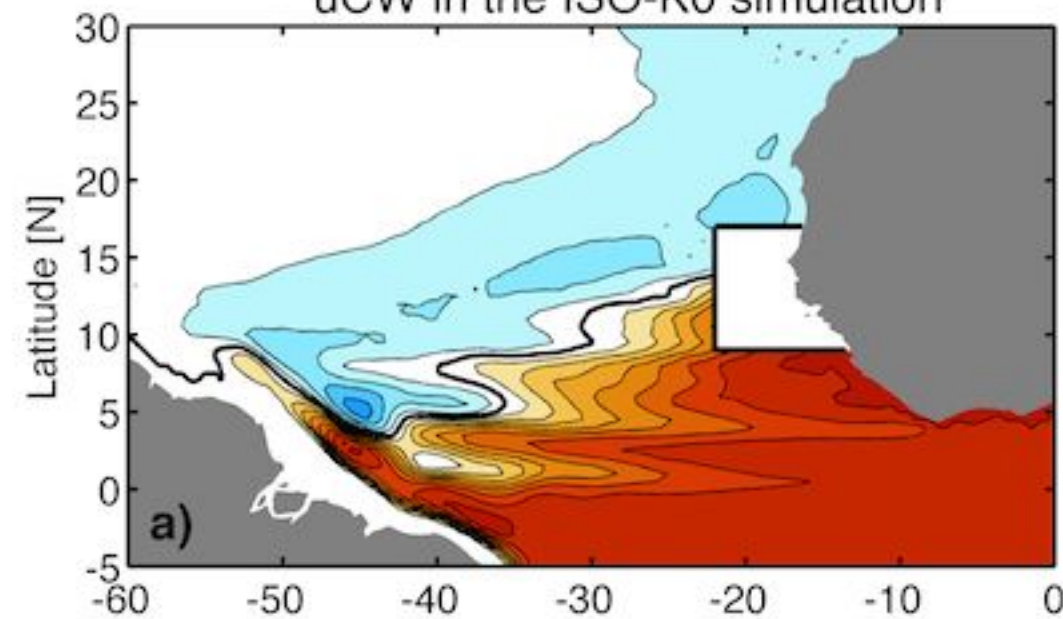


Std of NACW proportion at sigma0 27.1

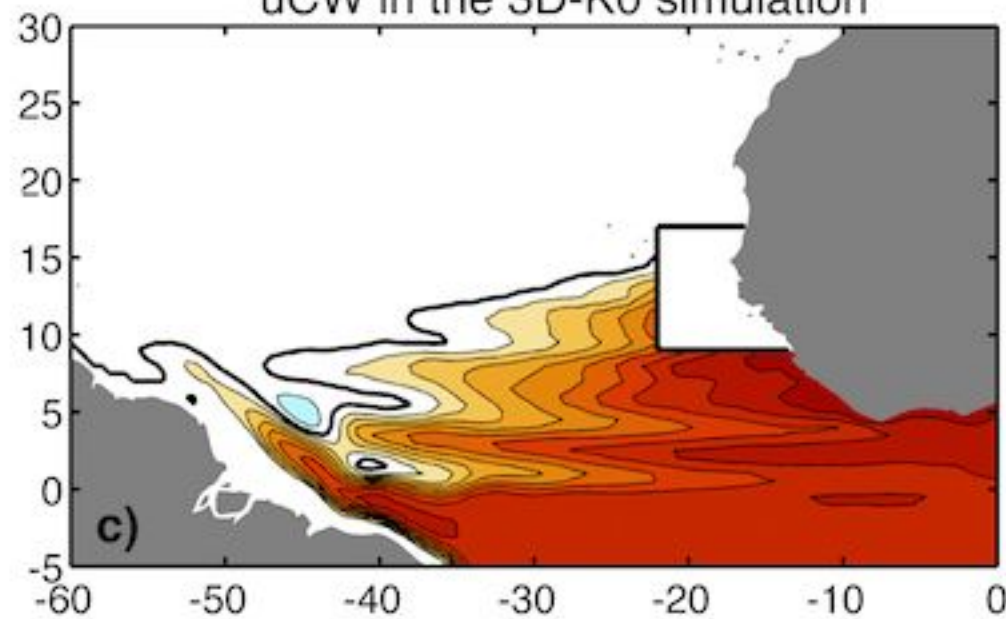




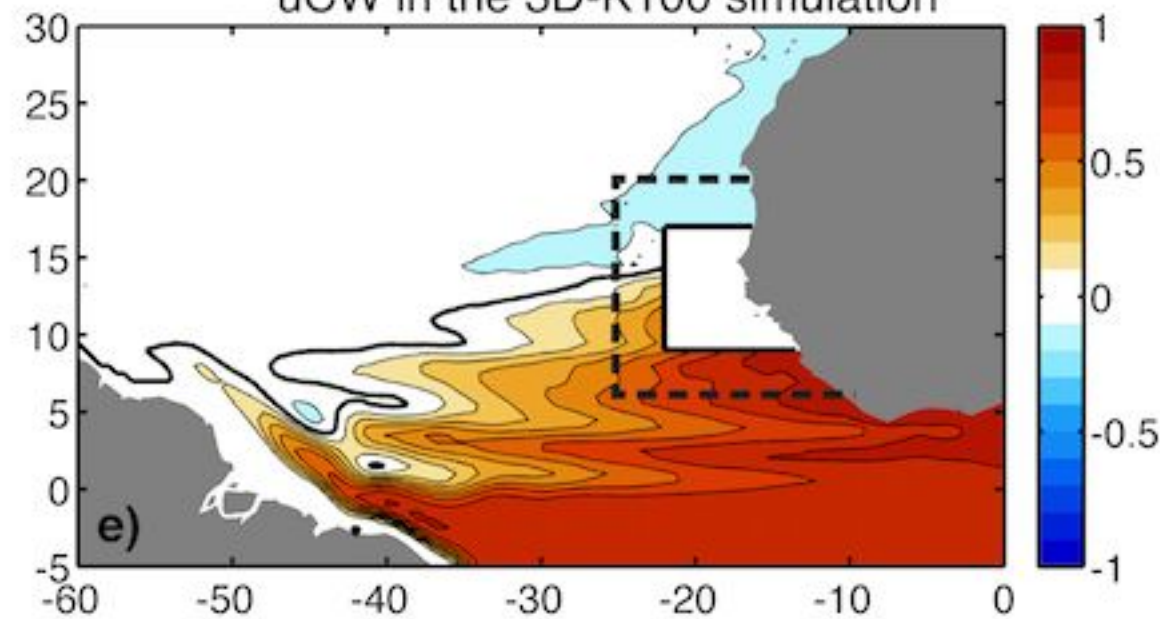
uCW in the ISO-K0 simulation



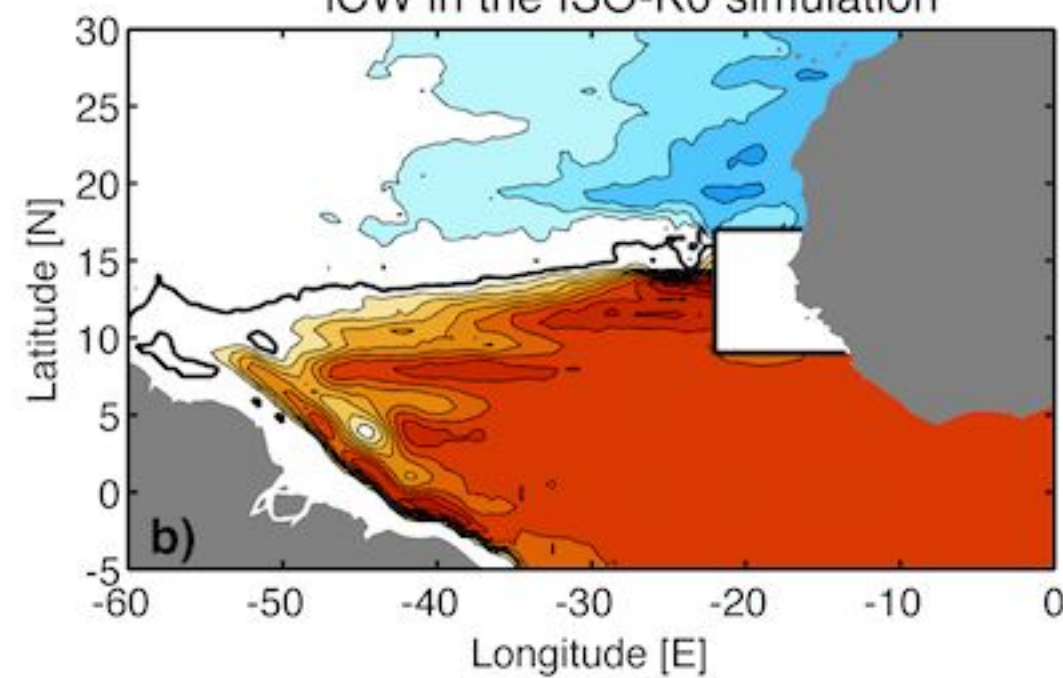
uCW in the 3D-K0 simulation



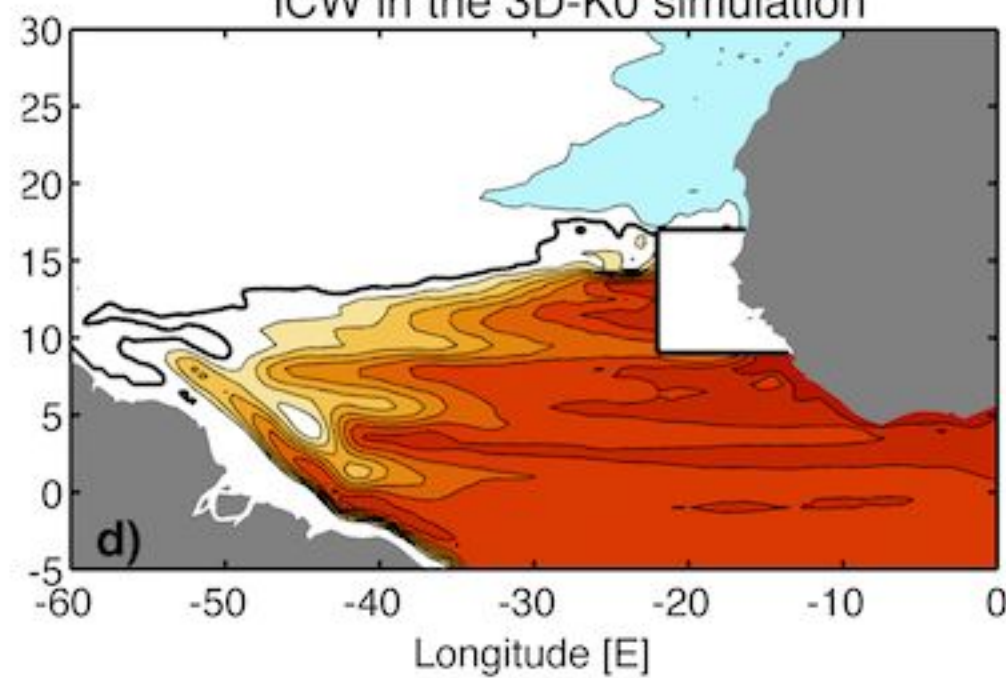
uCW in the 3D-K100 simulation



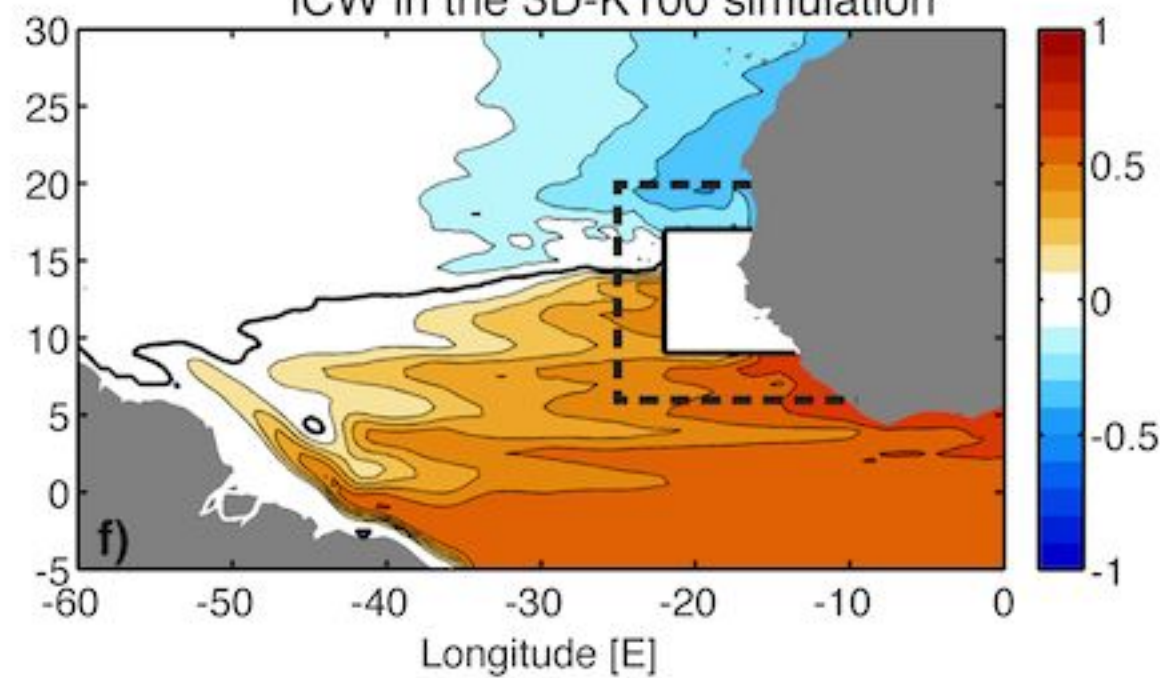
ICW in the ISO-K0 simulation



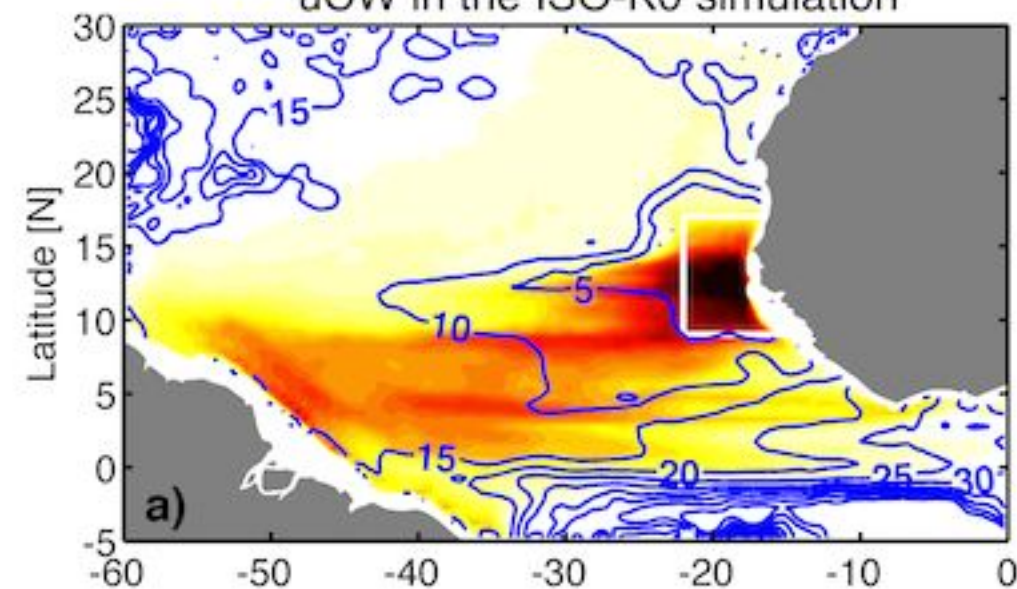
ICW in the 3D-K0 simulation



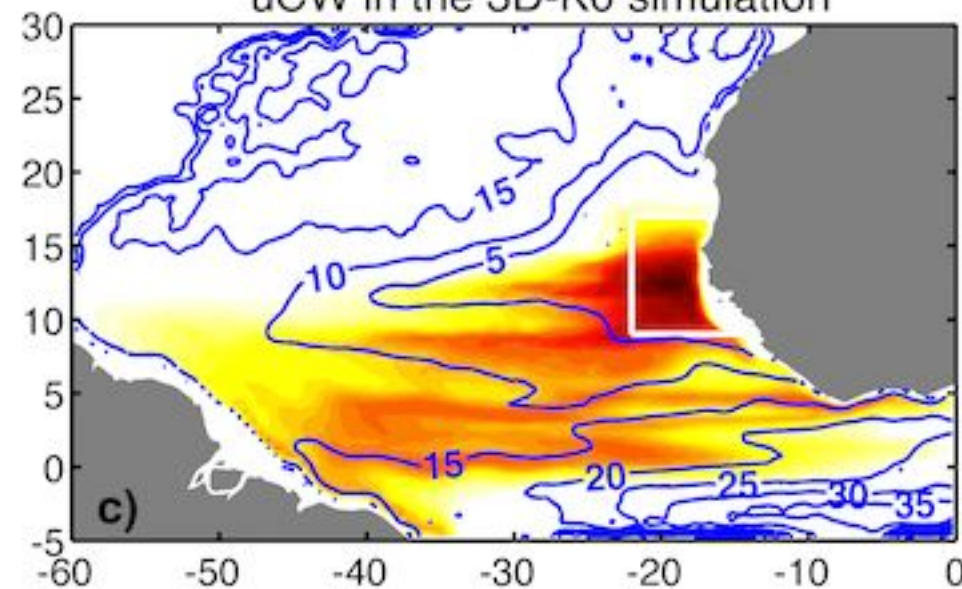
ICW in the 3D-K100 simulation



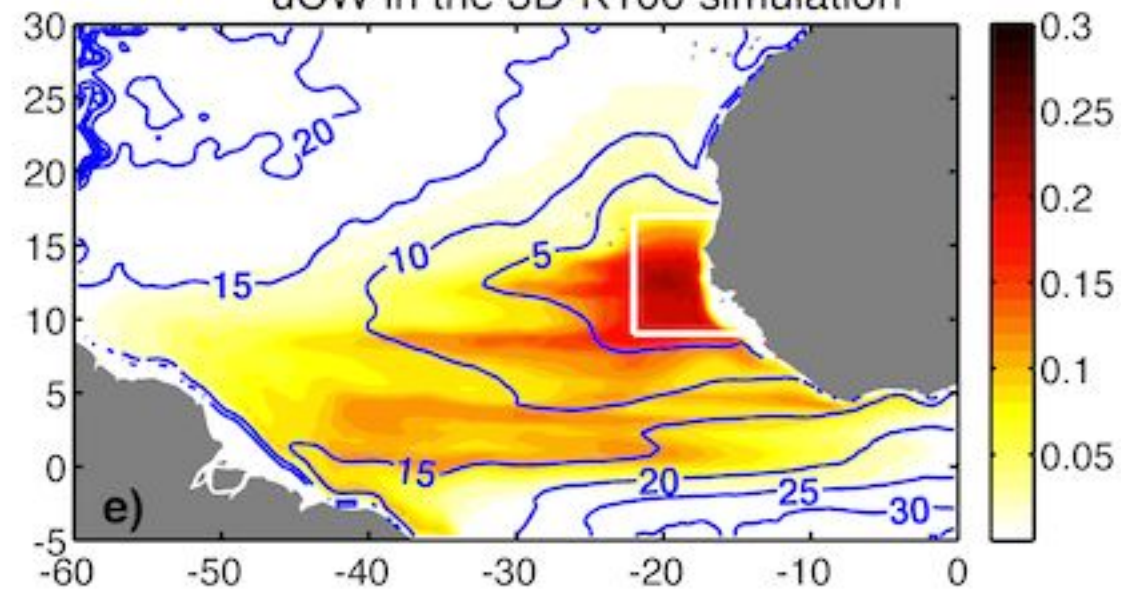
uCW in the ISO-K0 simulation



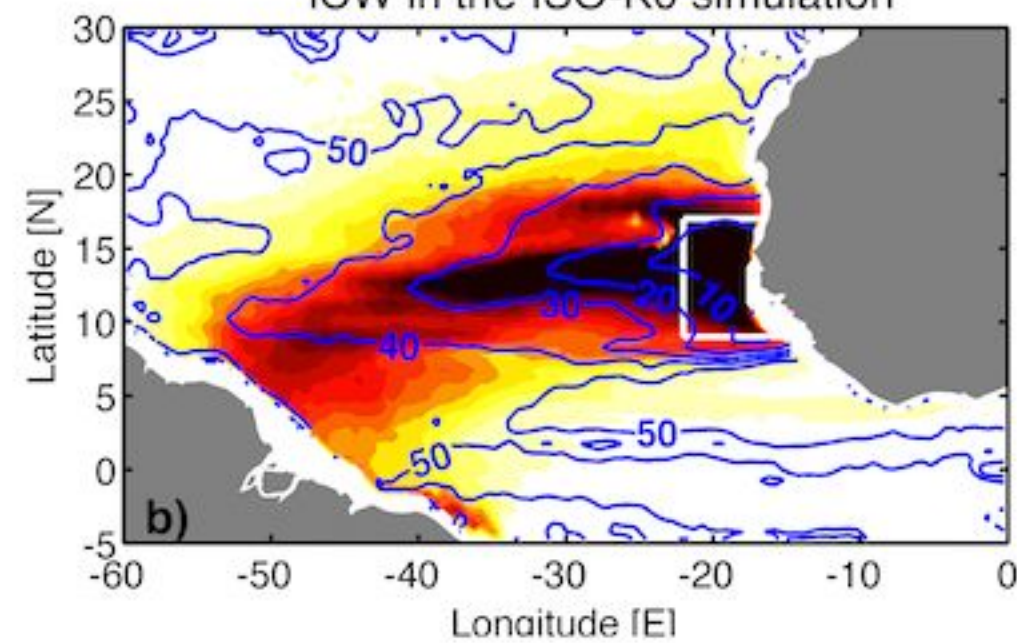
uCW in the 3D-K0 simulation



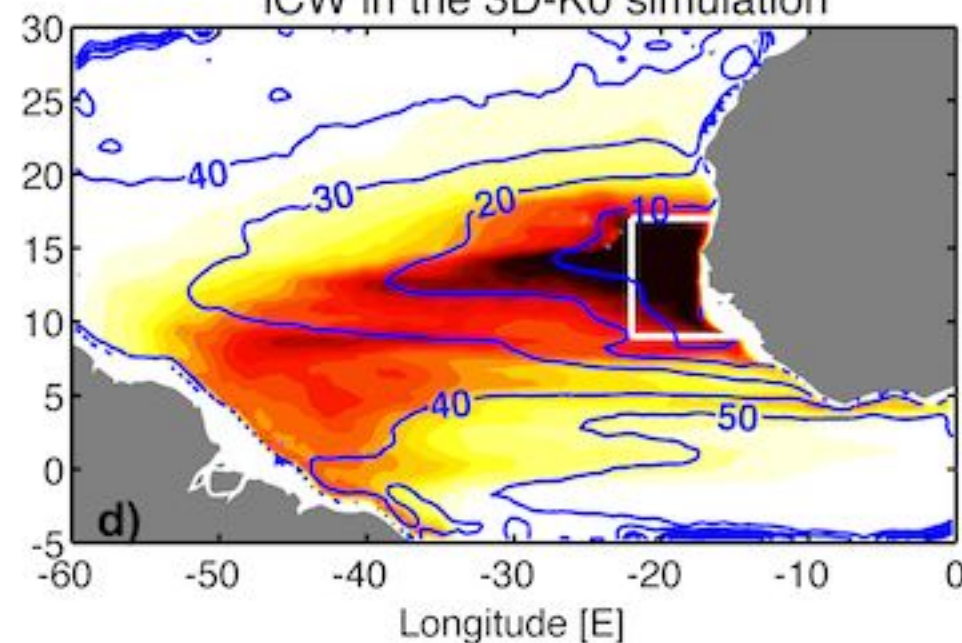
uCW in the 3D-K100 simulation



ICW in the ISO-K0 simulation



ICW in the 3D-K0 simulation



ICW in the 3D-K100 simulation

